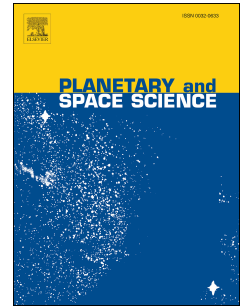# Accepted Manuscript

Biosignature detection by Mars rover equivalent instruments in samples from the CanMars Mars Sample Return Analogue Deployment

Jessica M. Stromberg, Alexis Parkinson, Matthew Morison, Edward Cloutis, Nora Casson, Daniel Applin, Jordan Poitras, Arola Moreras Marti, Catherine Maggiori, Claire Cousins, Lyle Whyte, Roman Kruzelecky, Debarati Das, Richard Leveille, Kim Berlo, Shiv K. Sharma, Tayro Acosta-Maeda, Michael Daly, Emmanuel Lalla

Please cite this article as: Stromberg, J.M., Parkinson, A., Morison, M., Cloutis, E., Casson, N., Applin, D., Poitras, J., Marti, A.M., Maggiori, C., Cousins, C., Whyte, L., Kruzelecky, R., Das, D., Leveille, R., Berlo, K., Sharma, S.K., Acosta-Maeda, T., Daly, M., Lalla, E., Biosignature detection by Mars rover equivalent instruments in samples from the CanMars Mars Sample Return Analogue Deployment, *Planetary and Space Science* (2019), doi: https://doi.org/10.1016/j.pss.2019.06.007.

1   **Biosignature Detection by Mars Rover Equivalent Instruments in Samples from**

2   **the CanMars Mars Sample Return Analogue Deployment**

3   Jessica M. Stromberg[a*], Alexis Parkinson[a], Matthew Morison[b], Edward Cloutis[a], Nora Casson[a],

4   Daniel Applin[a], Jordan Poitras[a], Arola Moreras Marti[c], Catherine Maggiori[d], Claire Cousins[c], Lyle

5   Whyte[d], Roman Kruzelecky[e], Debarati Das[f], Richard Leveille[f], Kim Berlo[f], Shiv K. Sharma[g],

6   Tayro Acosta-Maeda[g], Michael Daly[h], Emmanuel Lalla[h]

7

8

9   [a] Department of Geography, University of Winnipeg, Winnipeg, Manitoba, R3B 2E9, Canada

10   [b] Department of Geography, University of Waterloo, Waterloo, Ontario, N2L 3G1, Canada

11   [c] School of Earth and Environmental Sciences, University of St.Andrews, St Andrews KY16

12   9AJ, UK

13   [d] Department of Natural Resource Sciences, McGill University, Ste. Anne de Bellevue, Quebec,

14   H9X 3V9, Canada[e] MPB Communications Inc., 151 Hymus Boulevard, Pointe Claire, Quebec,

15   H9R 1E9, Canada

16   [f] Department of Earth and Planetary Sciences, McGill University, 3450 University Road, H3A

17   0E8 Montreal, Quebec Canada.

18   [g] Hawaii Institute of Geophysics and Planetology, University of Hawaii, 2525 Correa Rd., HIG,

19   Honolulu, HI 96822, USA

20   [h] Centre for Research in Earth and Space Science, York University, Toronto, 4700 Keele st., M3J

21   1P3, Canada

22   *Correspond author: jessica.m.stromberg@gmail.com

23

24

25

26

27

28

29

30

31

32

33

Abstract

This work details the laboratory analysis of a suite of 10 samples collected from an inverted

fluvial channel near Hanksville, Utah, USA as a part of the CanMars Mars Sample Return

Analogue Deployment (MSRAD). The samples were acquired along the rover traverse for

detailed off-site analysis to evaluate the TOC and astrobiological significance of the samples

selected based on site observations, and to address one of the science goals of the CanMars

mission: to evaluate the ability of different analytical techniques being employed by the

Mars2020 mission to detect and characterize any present biosignatures. Analytical techniques

analogous to those on the ExoMars, MSL and the MER rovers were also applied to the samples.

The total organic carbon content of the samples was <0.02 % for all but 4 samples, and organic

biosignatures were detected in multiple samples by UV-Vis-NIR reflectance spectroscopy and

Raman spectroscopy (532 nm, time-resolved, and UV), which was the most effective of the

techniques. The total carbon content of the samples is < 0.3 wt% for all but one calcite rich

sample, and organic C was not detectable by FTIR. Carotene and chlorophyll were detected in

two samples which also contained gypsum and mineral phases of astrobiological importance for

paleoenvironment/habitability and biomarker preservation (clays, gypsum, calcite) were detected

and characterized by multiple techniques, of which passive reflectance was most effective. The

sample selected in the field (S2) as having the highest potential for TOC did not have the highest

TOC values, however, when considering the sample mineralogy in conjunction with the

detection of organic carbon, it is the most astrobiologically relevant. These results highlight

importance of applying multiple techniques for sample characterization and provide insights into

their strengths and limitations.

Highlights

- Detection and characterization of organic carbon and biomolecules by multiple rover-
  equivalent instruments
- Detection and characterization of astrobiologically relevant mineral phases

62 • Application of lab-based techniques analogues to instrumentation from multiple rover
63 missions
64

65 **Keywords**
66 Mars Analogue; Fluvial Channel; Rover Instrumentation; Spectroscopy; Mineralogy;
67 Astrobiology
68

69 **1. Introduction**
70

71 One of the main scientific drivers of the exploration of Mars is the search for signs of life, past
72 and present, on or near the surface. To enable more effective utilization and operation of future
73 Mars rovers, an international team of researchers, scientists, and engineers undertook a field
74 campaign at a Mars analogue site near Hanksville, Utah, USA in October 2016. The site is
75 dominated by inverted fluvial channels and the mission was termed the CanMars Mars Sample
76 Return Analogue Deployment (MSRAD). The operational aspects of this program are described
77 in companion papers in this special issue and were based on the Phoenix and MER (Mars
78 Exploration Rover) missions using the Mars Exploration Science Rover (MESR) and a suite of
79 handheld and integrated instruments to mimic the Mars2020 rover payload (Caudill et al.,
80 2019a,b; Osinski et al., 2019; Pilles et al., 2019). Two of the main objectives of this deployment
81 was to assess the astrobiological significance of the field site in terms of organic carbon and
82 evidence of water, as well as the ability of different analytical techniques to be employed by the
83 Mars2020 rover to characterize targets of interest at the deployment site, more specifically how
84 well such instruments can characterize geological samples and detect and characterize any
85 biosignatures (Caudill et al., 2019; Osinski et al., 2019).
86

87 This study describes the characterization of a suite of 10 samples (termed the Hanksville 10)
88 which were acquired along the rover traverse (Figure 1) for detailed off-site analysis. The
89 rational for site selection, rover traverse, and rover sampling are described in detail in this issue
90 (Pilles et al., 2019; Caudill et al., 2019a,b), however, a major focus of this mission was to select
91 samples with high organic carbon contents as a first order proxy for the presence of preserved
92 biomarkers or extant life. This also addresses the astrobiology objectives of NASA's Mars2020

93 Rover and ESA's ExoMars Rover (Mars 2020 SDT, 2013; Farley and Willeford, 2017; Vago et

94 al., 2017). In this context, organic carbon refers to carbon which is bound to H and C in an

95 organic compound.

96

97 In this study, the Hanksville 10 sample suite underwent analysis by laboratory based

98 geochemical, mineralogical and spectral techniques comparable to those on past, present, and

99 future rovers including the Mars2020 mission (Table 1). The overarching goal of these analyses

100 was to assess the organic content of the samples selected by the rover-based operations team and

101 provide insights into ability of these analytical methods for detecting and characterizing the

102 presence of organic carbon, and for characterizing potentially habitable environments.

103

104 *1.1 Site Description*

105 The field site is located ~8km to the northwest of Hanksville, Utah in a desert climate on the

106 Colorado Plateau. The site consists of inverted fluvial sediments which represent an

107 anastomosing paleochannel existing as inverted features due to subsequent erosion of the

108 surrounding sediments (Figure 1; Miall and Turner-Peterson, 1989; Williams et al, 2009). The

109 stratigraphy is dominated by near flat lying sandstone and shales and exhumed from the Jurassic

110 age Brushy Basin Member of the Morrison Formation (Schweikert et al., 1984; Hintze and

111 Kowallis, 2009). The landscape is eroded resulting in the formation of mesas and scarp-bounded

112 surfaces where the clay rich layers are preferentially eroded with respect to the sandstones

113 (Clarke and Pain, 2004; Clarke and Stoker, 2011). The geology and characteristics of the

114 immediate site area are described in detail in Beatty et al., 2019 (this issue). The region sampled

115 corresponds to the SCYLD region of the rover traverse, a region containing the topographical

116 feature referred to as Ragnarok (Osinski et al., 2019), a large eroded mound of nearly flat lying

117 units of variable colored sediments (Figure 1).

118

119 *1.2 Mars Relevance*

120 The characterization of regions in which water flowed on Mars has been a historical driver for

121 exploration. More recently these locations have also been of great interest due to the potential

122 opportunity for biosignature preservation, detection, and characterization (e.g., Clarke and

123 Stoker, 2011). Fluvial and inverted fluvial channels are widely present on Mars from the

124   Noachian through Early Hesperian (e.g., Pain et al., 2007; Newsom et al., 2010; Balme et al.,

125   2015) and have been proposed to be present in Gale crater (Orgel et al., 2013), and several of the

126   proposed Mars 2020 and ExoMars landing sites (Balme et al., 2015). Given their geologic

127   history of water, fluvial channels are excellent targets for the detection of a diverse range of

128   geological and bio indicator materials and have also been considered as landing sites for past

129   missions including MSL (Marzo et al., 2009; Rice and Bell, 2010; Clarke and Stoker, 2011). The

130   history of water in these regions is integral for past habitability, and also may play a role in the

131   preservation of biomolecules in evaporite minerals (gypsum, calcite, halite) or as endolithic

132   communities (e.g., Summons et al., 2011; Stromberg et al., 2014; Baque et al., 2016).

133

134   In addition to the inverted fluvial channel component of the Hanksville site, the region locally

135   consists of clastic and chemical precipitates including mudstones, conglomerates, clays,

136   carbonates, and iron oxides (Battler et al., 2006; Hintz and Kowallis, 2009), all of which have

137   been detected on the Martian surface (e.g., Ehlmann et al., 2008; Williams et al., 2013). This in

138   conjunction with the arid and vegetation poor nature of the region makes the Hanksville site an

139   appropriate site to assess the application of rover comparable techniques for characterizing

140   habitability, and biomolecule preservation and detection in an inverted river channel

141   environment.

142
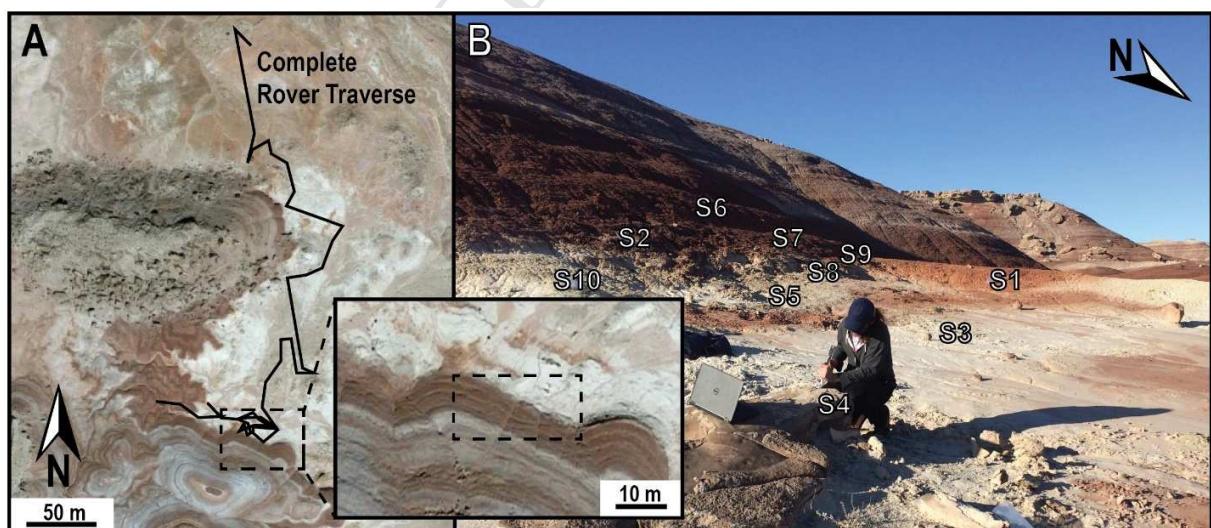
143

144   **Figure 1.** Sample context. A. Satellite image of the field area overlain with the entire rover

145   traverse. Inset zoomed in satellite image of the sampled area. B. Photo of the sampling area with

146   the sample locations labelled (S1-10).

147

148

149   **Table 1.** Analytical techniques applied to the Hanksville 10 sample suite and their lab based and

150   rover equivalents.

| Technique	Lab Instrument	Rover Instrument			
		Mars 2020	**ExoMars**	**MSL**	**MER**
LIBS	J200 LIBS	SuperCam	-	ChemCam	-
Raman	B&WTek i-Raman-532		RLS	-	-
Time Resolved Raman	Standoff Time Resolved Raman		-	-	-
UV-Vis-NIR Spectroscopy	ASD FieldSpecPro		PanCam, MA_MISS	Mastcam	PanCam
FTIR Spectroscopy	Bruker FTIR		MicroOmega, ISEM	-	Mini-TES
XRF	XRF (lithium tetraborate digestion)	PIXL	-	CheMin, APXS	APXS
Fe2+/Fe3+	Wet Chemistry	-	-	-	Mössbauer
UV Raman		SHERLOC	-	-	-
XRD	Bruker D8 Advance, Terra	-	-	CheMin	-

151

152

153

154   **2. Methods**

155

156   *2.1 Sampling and Sample Descriptions*

157   Ten samples (S1-10) were collected from along the rover traverse (Figure 1) using field photos

158   as a guide to select regions as close as possible to the rover sample locations (Caudill et al.,

159   2019a,b) (Table 2; Figure 2). The guiding principles for the rover samples sites are outlined in

160   Caudill et al. (2019a) and Pilles et al. (2019) with the primary objective being to test the

161   accuracy of selecting samples with high organic carbon content and the potential for biosignature

162 preservation using a rover-based operations team (Caudill et al., 2019a). The team used their

163 geological interpretations of the region as well as "rover" data to select sample locations.

164 Samples consist primarily of unconsolidated surficial material which was scooped into a sample

165 bag except for sample S4 which was hammered off a sandstone boulder (Figure 2).

166

167
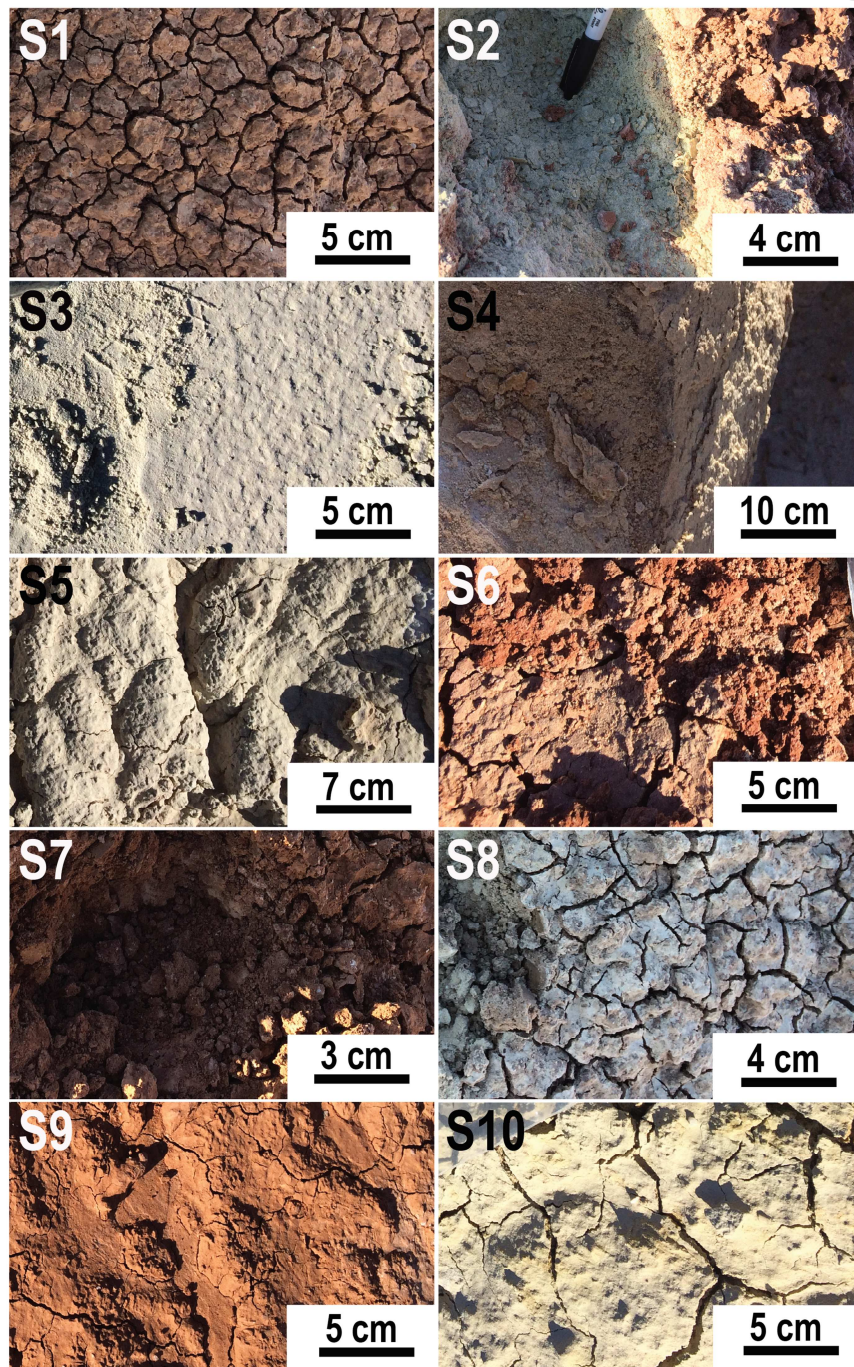
168 **Figure 2.** Photos of the sample locations for samples S1 – S10. The samples were taken next to

169 the rover traverse and are variable in color as well as texture, ranging from friable (e.g., S2) to a

170 cemented sandstone boulder (S4).

171

172

173 **Table 2**. Sample descriptions and the locations along the rover traverse and/or rover sample they

174 correspond to.

175

Sample ID	Description
S1*	Mud-cracked, friable, coarse-grained reddish-brown clay
S2	Unconsolidated, medium-grained green clay
S3	Unconsolidated, fine-grained white clay
S4	Sandstone boulder
S5	Fine-grained white clay
S6*	Mud-cracked, friable, red clay
S7*	Unconsolidated, coarse-grained red clay
S8*	Mud cracked, friable, greyish-green clay
S9	Unconsolidated, fine-grained red clay
S10	Mud-cracked, friable, yellowish clay

176 *Dried at 70°C*

177

178

179 *2.2 Sample Preparation*

180 Samples were pulverized and homogenized and subdivided into aliquots to ensure representative

181 data. Aliquots were dry sieved to a grain size of <1 mm (10 grams) with wet samples first dried

182 at 70°C overnight. The <1 mm aliquots were further crushed in alumina mortar and pestles and

183 dry-sieved to grain sizes of <150 µm and <45 µm. A summary of the sample aliquot and grain

184 size used for each analysis can be found in the supplementary data and was technique dependent

185 to allow for rover comparable datasets.

186

187 *2.3 Light Element Analysis*

188 Light element analysis (total C, N, and S) was undertaken at the University of Waterloo

189 Environmental Isotope Lab by Continuous Flow Stable Isotope Ratio Mass Spectrometery

190 (CFIRMS). Data for total organic carbon, nitrogen, and sulfur was collected from powdered

191 samples to provide ground truth data. Nitrogen and carbon abundances were determined through

192 combustion conversion (Elemental Microanalysis E3004 Separation Column NC/NCS 3m

193 Stainless Steel) to N_2 and CO_2 gases through a Costech Instruments Elemental Analyzer coupled

194 to a Delta[plus] XL Continuous Flow Stable Isotope Ratio Mass Spectrometer (Thermo Finnegan).

195 The %N and %C are bulk measurements based on sample weight against the following know

196 standard reference materials (EURO SOIL-5, NIST-2704, NIST-2711). Sulfur measurements

197 were determined through combustion conversion (Elemental Microanalysis E3002 Separation

198 Column Sulphur 0.8m PTFE) to SO_2 gas through a Costech Instruments Elemental Analyzer

199 (CHNS-O ECS 4010) coupled to an Isochrom (GVI / Micromass) Continuous Flow Stable

200 Isotope Ratio Mass Spectrometer. The %S element content (Total % column) is a bulk

201 measurement based on the sample weight against known certified elemental standard materials

202 (B2036 – suphanilamide) with values provided through the Commission on Isotopic Abundances

203 and Atomic Weights (CIAAW). Every 4th to 6th sample was repeated with no less than 20%

204 Std/Ref material. The detection limits were 0.005% for N, 0.008% for C and 0.4% for S, and

205 error in the measurements wa ±0.01 for N, ±0.02 for C, and ±0.2 for S.

206

207 The samples were acid-washed to remove inorganic carbon and re-analyzed for TOC using the

208 method described above. The acid wash involved the addition of ~2-5% HCl to the sample

209 followed by heating to <60ºC for 90 minutes. This is repeated until the pH level of the remains

210 acidic. The sample is then left to settle, and the water is decanted (aspirated) off. The sample was

211 rinsed with nan-pure water, allowed to settle, then the water was removed. This was repeated 3-5

212 times and with the final rinse the sample was dried overnight in a freeze-drier.   The error on the

213 TOC measurements was ±0.03 %.

214

215 *2.4 X-Ray Diffraction (XRD)*

216 *2.4.1 Lab based Powder XRD*

217 XRD data was acquired in continuous scan mode from 5 to 80º 2θ on a Bruker D8 Advance with

218 a DaVinci automated powder diffractometer of <45 μm sample aliquots. It uses a Bragg-

219 Brentano goniometer with a theta-theta setup was equipped with a 2.5º incident Soller slit, 1.0

220 mm divergence slit, a 2.0 mm scatter slit, a 0.6 mm receiving slit, a curved secondary graphite

221 monochromator. Diffracted X-rays were collected by a scintillation counter collecting at an

222   increment of 0.02º and integration time of 1 second per step. The line focus Co X-ray tube was

223   operated at 40 kV and 40 mA, using a take-off angle of 6º. Diffraction patterns were interpreted

224   using Bruker Diffracsuite EVA software and the International Center for Diffraction Data

225   Powder Diffraction File (ICDD-PDF-2) database.

226

227   *2.4.2 Portable XRD*

228   X-ray diffraction data of samples crushed to <150 µm was collected using a portable InXitu

229   Terra 299 X-ray instrument. This instrument has a 1024 x 256 pixel – 2D Peltier-cooled CCD

230   (charge coupled device) detector providing continuous scans from 5 to 55° 2θ collecting at an

231   increment of 0.05° for XRD. The Cu source X-ray tube was operated at 30kV offering 10 W of

232   power.

233

234   *2.5 Reflectance Spectroscopy*

235   *2.5.1 Ultraviolet-visible-near infrared reflectance spectra (UV-VIS-NIR, 350-2500 nm)*

236   Long wave ultraviolet, visible and near IR (350-2500 nm) reflectance spectra of the <1mm and

237   <150µm sample aliquots was measured with an Analytical Spectral Devices (ASD) FieldSpec

238   Pro HR (high resolution) spectrometer. This instrument has a spectral resolution between 2 and 7

239   nm (internally resampled by the instrument to 1nm). Spectra were collected at a viewing

240   geometry of $i = 30º$ and $e = 0º$ with incident light being provided by an in-house 150 W quartz-

241   tungsten-halogen collimated light source. Sample spectra were measured relative to a

242   Spectralon® 100% diffuse reflectance standard and corrected for minor (less than ~2%)

243   irregularities in its absolute reflectance. 200 spectra of the dark current, standard, and sample

244   were acquired and averaged, to provide sufficient signal-to-noise for subsequent interpretation.

245   Some spectra show occasional small reflectance offsets at 1000 and 1830 nm because the fiber

246   optics that feed the three detectors in the ASD do not view the exact same spots on the sample.

247   These offsets are corrected by scaling the short (350-1000 nm) and long wavelength (1830-2500

248   nm) detectors to the end points of the central detector, which is temperature controlled.

249

250   *2.5.2 Diffuse Mid- Infrared reflectance spectra (2.5-5.2μm)*

251   Diffuse reflectance spectra were collected with a Bruker Vertex 70 Fourier Transform Infrared

252   (FTIR) spectrometer using a 20-watt infrared Globar light source, mercury cadmium

253 telluride (MCT) cryo-cooled detector and KBr broadband beamsplitter over the wavelength

254 range of 2.0–20.0 μm. Reflectance spectra were acquired relative to a Labsphere Infragold®100%

255 reflectance standard measured at $i = 30°$ and $e = 0°$ using a SpecAc Monolayer grazing angle

256 specular reflectance accessory. A total of 1500 spectra were collected at a scanner velocity of 40

257 kHz and were averaged to improve SNR (signal to noise ratio). All measurements were made

258 using an identical viewing geometry, integration time, and number of averaged spectra.

259

260 *2.6 Bulk Rock Geochemistry*

261 Bulk rock geochemistry was determined by laboratory X-ray fluorescence (XRF) as a proxy for

262 the PIXL instruments XRF capabilities. XRF analysis were undertaken at the X-Ray laboratory

263 at Franklin and Marshall College where rock powder (0.4000 grams) was mixed with lithium

264 tetraborate (3.6000 grams), and placed in a 95% platinum, 5% gold crucible and heated with a

265 Meeker furnace until molten. The molten material was transferred to a platinum casting dish and

266 quenched. This produces a glass disk that was used for XRF analysis of major and selected

267 minor elements. Elemental abundances were converted to equivalent oxides using the normal

268 oxidation state of the various elements. Trace elements (Sr, Zr, V, Cr, Ni, and Co) are reported as

269 parts per million. Working curves for each element were determined using rock geochemical

270 standards (Abbey, 1983). The curve was made up of 30-50 data points with various elemental

271 interferences considered. Results were calculated and presented as percent oxide, and standard

272 deviations are all less than ±0.15 wt% with an average of ±0.3 wt%. Details of the methods can

273 be found in Mertzman (2000).

274

275 Ferrous iron was determined by titration using a modified Reichen and Fahey (1962) method.

276 Ferric iron (Fe^{3+}) wass determined as the difference between total Fe by XRF and ferrous iron.

277 Loss on ignition was determined by heating an exact aliquot of the samples at 950°C in air for

278 one hour and measuring resultant weight loss.

279

280

281 *2.7 Laser Induced Breakdown Spectroscopy (LIBS)*

282 LIBS measurements were collected using J200 Laser Induced Breakdown Spectroscopy

283 instrument from Applied Spectra Inc. using a 213 nm Nd- YAG laser operated at a 10Hz

284   repetition rate and 5 ns pulse duration at McGill University. This LIBS instrument has a Czerny

285   Turner spectrometer with a 1200 diffraction grating. Flat, but unprocessed surfaces of nine

286   samples of consolidated material (2-3mm) were analyzed. To mimic the broadband capability of

287   the ChemCam instrument, measurements were taken at three wavelength ranges: the UV range

288   between 225 and 350 nm, the violet & blue range between 365 and 480 nm, and the visible range

289   between 555 and 657 nm at a spectral resolution of 0.1 nm/pixel. The laser output energy was

290   1.275 mJ/pulse. Analyses were conducted in air with a gate delay of 0.4 μ s and a gate width of

291   3 μ s. Bulk analyses were conducted by rastering the surface of the samples. Each raster consists

292   of 800 shots covering a grid of approximately 0.5 x 0.5 mm. The spectra were normalized to

293   their total intensities and averaged to correct for fluctuations in laser energy and sample

294   inhomogeneity The normalized and averaged LIBS spectra were plotted against relative

295   intensities using the Aurora software and peaks were identified using the NIST LIBS database

296   (https://physics.nist.gov/PhysRefData/ASD/LIBS/libs-form.html).

297

298   *2.8 Raman Spectroscopy*

299   *2.8.1 iRaman 532nm*

300   Raman spectra were collected from multiple spots on both whole rock and powdered (<45μm)

301   samples using a B&WTek i-Raman-532-S instrument in the Raman shift range of 175-4000 cm^{-1}.

302   This was done with a spectral resolution of ~4 cm^{-1} at 614 nm with a 532nm excitation energy

303   provide by a ~50mW solid state diode laser. Raman-scattered light was detected by a Glacier^{TM}

304   *T*, a high spectral resolution (0.08 nm) thermoelectrically cooled (14°C) CCD detector. The

305   automatic integration time function (which increases integration time incrementally, until the

306   response is close to saturation) was used, yielding an optimal SNR. Measurements for each

307   sample were made by first acquiring a dark current spectrum, followed by measurement of the

308   sample. Both measurements were made using an identical viewing geometry, integration time,

309   and number of averaged spectra. Raman-shift calibration was monitored through regular

310   measurements of a polystyrene standard. The RRUFF^{TM} database was used for peak

311   identification (Downs et al., 2015).

312

313   *2.8.2 Time-Resolved Raman*

314 Powdered samples were analyzed with a time-resolved standoff Raman spectrometer with 532

315 nm pulsed excitation (Nd:YAG, 20Hz rep rate, 30mJ/pulse) at the Hawai'i Institute of

316 Geophysics and Planetology Raman Systems Laboratory (Sharma et al., 2002; 2007). Integration

317 times range from 1-20 pulses on the ICCD (intensified charge coupled device) detector

318 (intensified and gated, 1408x1044 pixels, 7x7um pixel, Syntronics) and 1-600 spectra were co-

319 added to improve resolution. Samples were run with an intensifier gain of 95%, gate time of 40ns

320 and a laser power of 10 mJ per pulse. The experimental parameters for each sample are detailed

321 in the Supplementary Materials.

322

323 *2.8.3 Ultra-Violet (UV) Raman*

324 For UV-Raman the samples were pressed into pellets (13 mm diameter, 3 mm thick) with a

325 pressure of 10 tons (Presser, Pike Technologies), which were then glued to standard microscope

326 slides to ensure their stability. The 266 nm Raman spectrometer at York is designed to fulfill the

327 future requirements of flight instrument concept tested on a breadboard system. The laser

328 excitation is provided by an ALPHALAS diode-pumped solid state Nd:YAG laser with a 0.6 ns

329 pulse width and 1:4 μJ of energy per pulse. The 1064 nm fundamental wavelength is frequency

330 quadrupled to obtain the desired 266 nm radiation with a laser pulsed of 5 kHz. The radiation

331 from the laser to sample travels through an optical system composed by four mirrors, one UV

332 coated beam expander and finally focused with an off axis parabolic mirror onto the sample

333 adding a path of ~2 m. The light scattered from the sample is focused trough a 10 cm telescope

334 into 8 meters UV-fiber coupled to an Andor Mechelle spectrometer allowing to observe from

335 240 to 900 nm. A 266 nm edge filter is installed at the fiber entrance to avoid the camera

336 saturation and cut the main laser wavelength.

337

338 The Raman signal is detected by an intensified CCD (Andor iStar) coupled to the spectrometer

339 and cooled to -20ºC. To compensate the delay on the system, an external photodiode is installed

340 at the first mirror triggering the spectrometer-camera system with the laser. The light entering the

341 detector is directed onto an 18 mm photocathode, generating photoelectrons which are amplified

342 in an intensifier tube. A phosphor converts the intensified electron cloud into visible photons

343 detectable by the 1024x1024 pixel CCD with 13 μm pixels approximately. The ICCD provides

344 nanosecond scale gating by controlling the voltage across the intensifier, allowing for reduction

345 of both ambient light and reduction of fluorescence, which typically has a longer lifetime than
346 Raman scattering.

347

348 A NIST (National Institute of Standards and Technology) calibrated deuterium lamp is used for
349 spectral intensity calibration of the spectrometer allowing to remove the effect of the edge filter
350 and saw tooth effect of the echelle spectrometer system. The wavelength calibration is done by
351 HgAr fiber coupled lamp from 240 nm to 890 nm following the standard procedure of the
352 manufacturer. The samples BC4S_X_i (X_i from 1 to 11) were measured at a distance of 20 cm
353 from the telescope following the LiRs Bread-board conditions. The samples were installed in a
354 mobile stage system to carry a total of 8 point in a line separated 1 mm per samples. Variation on
355 the acquisition in exposition time and accumulations from 1 minute to 1 hour have been done
356 depending on the sample and SNR achieving the best signal possible. The standard measurement
357 for almost all the samples was around from 15 to 20 min, however in some case the measurement
358 were done up to 1 hour.

359

360 The spectra was manually REC corrected, and post background processed with a polynomial
361 fitting and a smoothing process of 5% FFT filtering. The saw tooth effect was minimized by one
362 spline correction on the baseline using 50 to 60 points. The Raman peak positions were
363 determined by Gaussian profiling using spectral commercial software packages and peak
364 identification was done by consultingthe RRUFF database spectra collection as well as the
365 relevant literature; Fe-oxides (Jubb and Allen, 2010; Rull et al., 2007), Ti-oxides (Lukačević et
366 al., 2012; Sekiya et al., 2001), Si-oxides (Karwowski et al., 2013; Zotov et al., 1999), carbonates
367 (Buzgar and Apopei, 2009; Koura et al., 1996), sulfates (Buzgar et al., 2009; Chio et al., 2005),
368 silicates (Freeman et al., 2008), zeolites (Chen et al., 2007; Frost et al., 2014) and clays (Frost et
369 al., 2001; Haley et al., 1982; Martens et al., 2002), organics (Daly. 2015; Huang et al., 2010).

370

371

372 **3. Results**

373

374 *3.1 Ground Truth TOC and Light Elements*

375   The TOC of the Hanksvilles samples is near the detection limits for the laboratory analysis

376   (0.008%) and several samples (S5,9) fall below the detection limits (BDL). TOC values range

377   from BDL to 0.07% in sample S4 which was from the consolidated sandstone boulder, with the

378   bulk of the samples in the 0.01 – 0.02% range (Table 3). The average total percent C, N and S

379   values are 0.240 ± 0.532 %, 0.103 ± 0.288 % and 0.438 ± 0.598 % respectively (Table 3), and

380   there is no significant correlation (r^2 <0.1) between sample total N, C and S. The highest C, S

381   and S values are found in samples S2 for total C (0.23%), sample-S2 for total N (0.97%), and

382   S10 for total S (1.73%). These values are an order of magnitude higher than for the other

383   samples.

384

385   *3.2 Mineralogy*

386   *3.2.1 X-Ray Diffraction*

387   The mineralogy of the Hanksville samples is dominated by quartz and a clay phase (nontronite

388   and/or montmorillonite). Minor/trace phases detected include calcite, gypsum, albite, and

389   anatase. An example of a typical diffraction pattern is shown in Figure 3. In general, the data

390   between the portable Cu-source instrument (Terra) is comparable to the laboratory-based Co-

391   source (Bruker) instrument. However, for samples S2,6,7,8 and 10 the diffraction patterns

392   collected in the lab have low counts and signal:noise ratio (Figure 3). This appears to be related

393   to high clay content with can cause preferred orientation effects due to the platy nature of clay

394   mineral. Despite the low counts the major phases and minor phases in the sample are still

395   detectable and are summarized in Table 3.

396

397
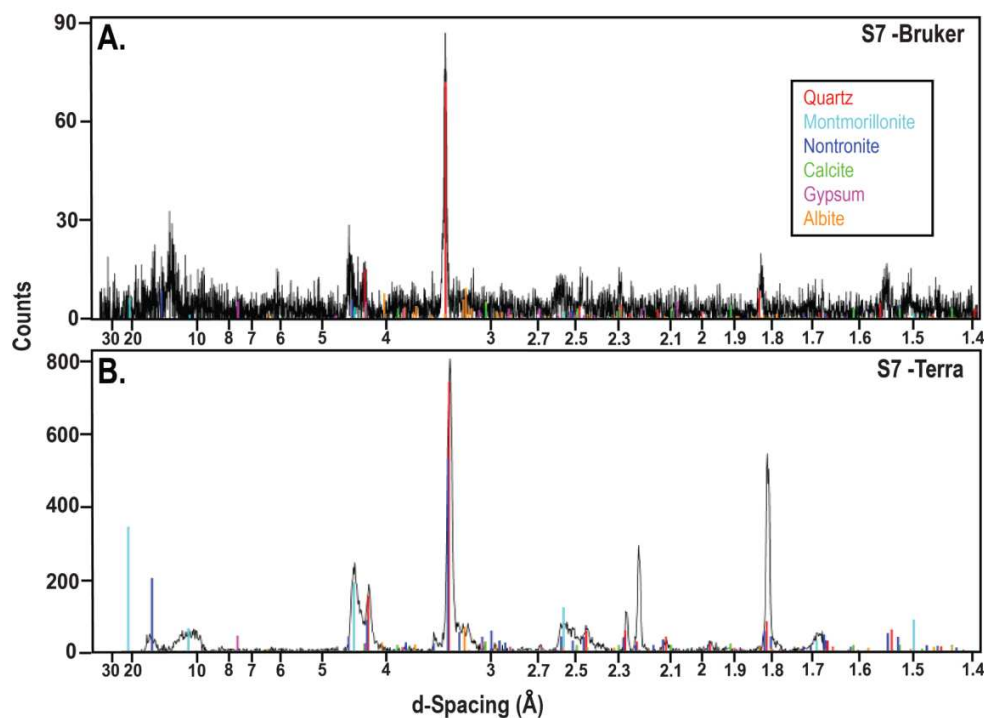
Figure 3. Comparison of field portable (Terra – Cu source) and laboratory (Bruker – Co source)

X-ray diffraction data for sample 7

400

3.2.2 Reflectance Spectroscopy

The UV-Vis-NIR (350 – 2500 nm) reflectance spectra of all samples is dominated by OH and

H_2O overtones and combinations (~1400, ~1900 nm), metal-OH overtones (~2100-2300 nm) and

Fe^{2+} and Fe^{3+} crystal field transitions (850, 1250 nm and steep drop below 800 nm) (Figure 4).

This reflects the presence of phyllosilicate phases (phengite and montmorillonite) in the samples.

These absorption bands occur in every sample with variable depths, however, there are several

other features which are unique to specific samples and are due to more minor, yet

astrobiologically important mineral phases and biomarkers. The most prominent of which is the

presence of a characteristic chlorophyll absorption band at ~670 nm in samples S3 and S4 (e.g.,

Figure 4). These two samples also show weak features below the 670 nm chlorophyll band which

are likely due to carotenoids. All the samples show evidence for more than one type of OH

overtone and combination from structural water in the 1400 nm and 1900 nm regions in the form

of a doublet or triplet. All the sample but S10 have a doublet, and S10 has a triplet which is

characteristic of the presence of gypsum. The Al-OH and Metal-OH absorption features as well

415   as Fe transitions (Figure 4,5) are characteristic of a phyllosilicate phase, likely nontronite and/or

416   montmorillonite. A carbonate overtone at ~2350 nm is also observed in samples S3, 4, 5, 10,11.

417   While the absolute reflectance of the finer of the two grain size sample aliquots (<150 um) is

418   higher than for the 1 mm aliquot, there is no change in the position or strength of absorption

419   features (Figure 5). The UV-Vis-NIR portion of the spectrum was stitched to the FTIR date to

420   cover the range of the CRISM spectrometers (up to 5200 nm). The IR region of the spectra

421   (~2500-5200 nm) is dominated by water absorption absorptions features at ~ 2700 nm and ~3000

422   nm. There are also characteristic absorption bands of carbonates at ~3500 and 4000 nm and of

423   sulphate at 4500 nm. The band depths of the 3780-4100 nm carbonate feature has been

424   quantified and compared to the calcite content of the samples (as calculated from C content)

425   indicating that calcite becomes detectable at concentrations of ~0.5-1% (Figure 6)

426

427

428
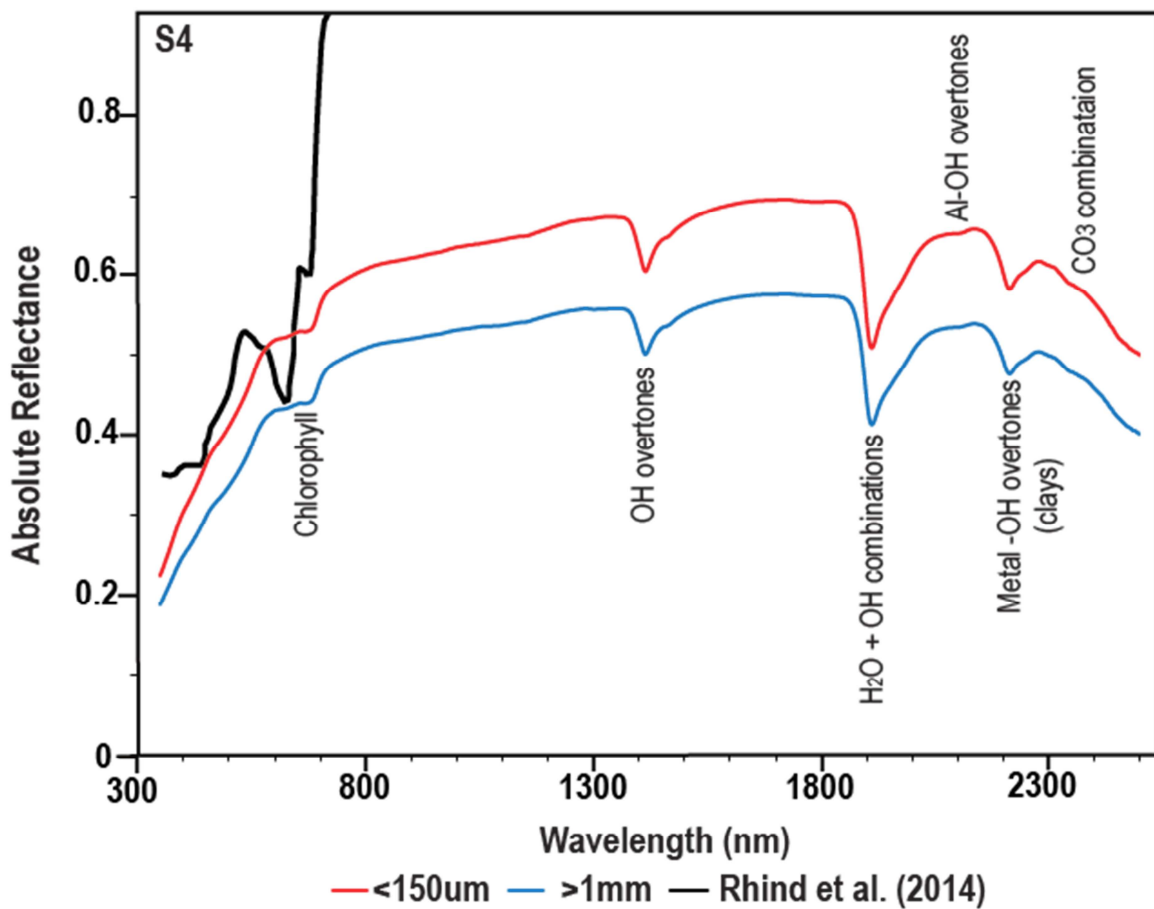
429 **Figure 4.** Ultraviolet–visible-near infrared (UV–vis-NIR, 350–2500nm) reflectance spectra of

430 sample S4 is dominated by features characteristic of montmorillonite and has the strongest

431 chlorophyll absorption feature (~670 nm). A reference spectrum of chlorophyll from Rhind et al.

432 (2014) is overlain. The absorption features are consistent between grain sizes despite the higher

433 absolute reflectance of the <150 μm grain size.

434

435

436

437

438
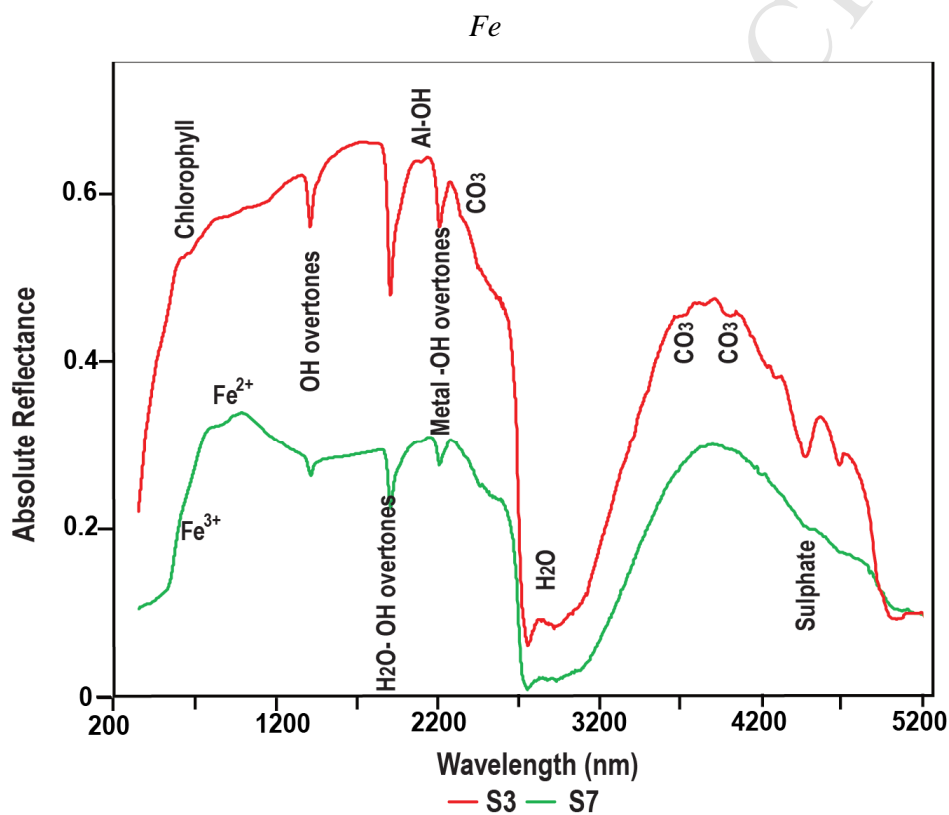
439 **Figure 5.** Stitched ultraviolet–visible-near infrared (UV–vis-NIR, 350–2500nm) and Infrared

440 (IR, 2500-5200 nm) reflectance spectra of sample S3 and S7. The spectrum is dominated by a

441 large water absorption at ~ 2500 nm. The samples show variability in the depth of the absorption

442 features from CO_3 (~2300, 3500, 3900 nm), OH overtones (~1300 nm), H_2O-OH combinations

443 (~1900 nm), metal-OH overtones (~2200 nm) and Fe^{2+} and Fe^{3+} transitions (~850, 1250, < 800

444 nm). Both spectra are dominated by features characteristic of montmorillonite, and sample S3

445 has a chlorophyll absorption feature at ~ 670 nm.

446
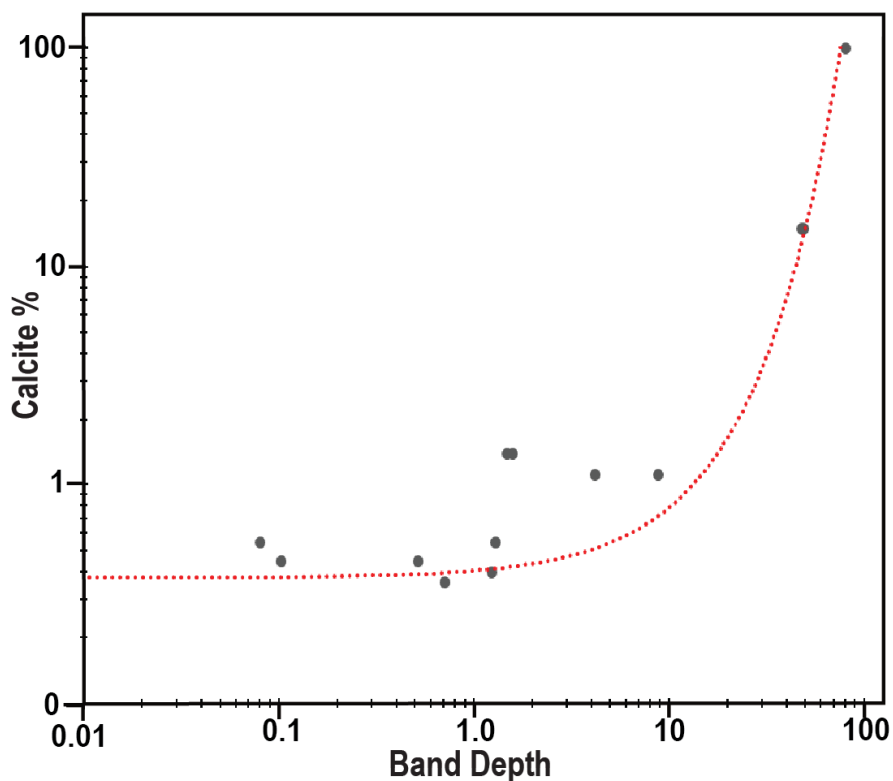
447

448 **Figure 6.** Plot of "calcite equivalent" % vs. band depth of the 3780-4000 nm CO_3 feature for

449 samples with >0% band depths indicates that calcite becomes detectable above ~0.5-1.0 weight

450 % as the samples with 0% band depth have "calcite equivalent" of up to 0.4 weight %.

451

452 *3.3 Geochemistry*

453 *3.3.1 X-Ray Fluorescence*

454 The XRF bulk rock geochemistry of the 10 samples is summarized in Table 3. The most

455 abundant major oxide is SiO_2 with an average of 73.30 ± 10.70 wt% and values as high as 94.89

456 wt% (S4). The samples also contain 11.07 ± 0.18 wt% Al_2O_3. The remainder of the major oxides

457 are present at a few weight percent level at most. The SiO_2 content of the samples correlates

458 negatively with TiO_2, Al_2O_3, Fe_2O_3, MgO, SO_3 with $r^2 > 0.75$. When plotted on an ACN-K

459 ternary diagram for weathering of clastic rocks (Nesbitt and Young, 1984), the samples cluster

460 towards the weathering trend of a felsic to intermediate igneous protolith to smectite (Figure 7).

461 This is also reflected in abundance of the Al-rich smectite (montmorillonite) detected in the

462 spectral and XRD data.

463

464

465

466

467

468

469

470

471

472

473

474

475 **Table 3.** Bulk rock geochemistry results for major and trace elements including % C, N, and S,

476 and XRD mineralogy results (Qtz – Quartz, Mnt – Montmorillonite, Non – Nontronite, Cal –

477 Calcite, Gyp – Gypsum, Alb – Albite)

ID	S1	S2	S3	S4	S5	S6	S7	S8	S9	S10
SiO_2	73.66	65.9	93.26	94.89	91.59	69.51	72.45	77.52	83.94	68.67
TiO_2	0.45	0.5	0.08	0.07	0.14	0.51	0.4	0.38	0.29	0.57
Al_2O_3	14.14	19.06	3.66	2.42	4.35	17.67	14.98	12.87	8.1	15.06
$Fe_2O_3T^1$	*3.82*	2.58	0.37	0.27	0.42	2.93	3.61	2	1.87	3.62
MnO	0.032	0.04	0.03	0.02	0.04	0.04	0.04	0.03	0.04	0.03
MgO	2.71	4.46	0.4	0.29	0.67	3.58	3.01	2.42	1.26	2.62
CaO	0.93	0.34	0.25	0.48	0.61	0.67	1.49	1.07	0.54	4.02
Na_2O	2.23	5.4	0.63	0.4	0.81	2.7	2.16	2.41	1.36	1.55
K_2O	1.792	1.32	1	0.82	1.13	1.91	2.48	0.96	2.08	3.44
P_2O_5	0.058	0.17	0.05	0.19	0.1	0.12	0.12	0.07	0.1	0.2
SO_3	0.17	0.13	0.06	0.01	0.1	0.07	0.07	0.11	0.09	0.22
Total[2]	99.992	99.9	99.88	99.95	99.96	99.71	99.81	99.85	99.67	100
LOI[3]	8.75	15.61	1.85	1.37	2.24	6.55	6.66	11.8	2.07	7.78
FeO[4]	0.18	0.18	0.06	0.05	0.13	0.14	0.15	0.1	0.12	0.18
Fe_2O_3[4]	3.62	2.39	0.3	0.21	0.28	2.77	3.44	1.89	1.74	3.42
Rb*	80	46	23	16	32	62	57	30	77	168
Sr*	238	90	164	161	284	122	782	355	387	325
Zr*	262	418	137	164	175	405	262	288	250	252
V*	60	57	26	21	39	54	52	71	44	86
Cr*	50	50	37	45	43	63	42	42	55	107
Co*	<1	38	<1	<1	<1	<1	<1	<1	<1	<1
%C	0.06	0.08	0.08	0.23	0.13	0.06	0.06	0.06	0.02	0.03
%TOC	0.01	0.02	0.02	0.07	bdl	0.01	0.02	0.01	bdl	0.01
%N	0.02	0.97	0.01	0.03	0.01	0.02	0.02	0.01	0.01	0.044
%S	0.101	0.94	bdl	0.07	bdl	0.07	0.33	0.20	0.07	1.73
Major	Qtz, Mnt	Mnt	Qtz	Qtz	Qtz	Qtz, Mnt, Non	Qtz, Mnt, Non	Qtz, Mnt, Non	Qtz, Mnt	Qtz, Mnt
Minor	Gyp	Qtz	Mnt		Non	Gyp	Cal, Alb, Gyp	Gyp	Alb	

478 [1]All Fe reported as Fe_2O_3
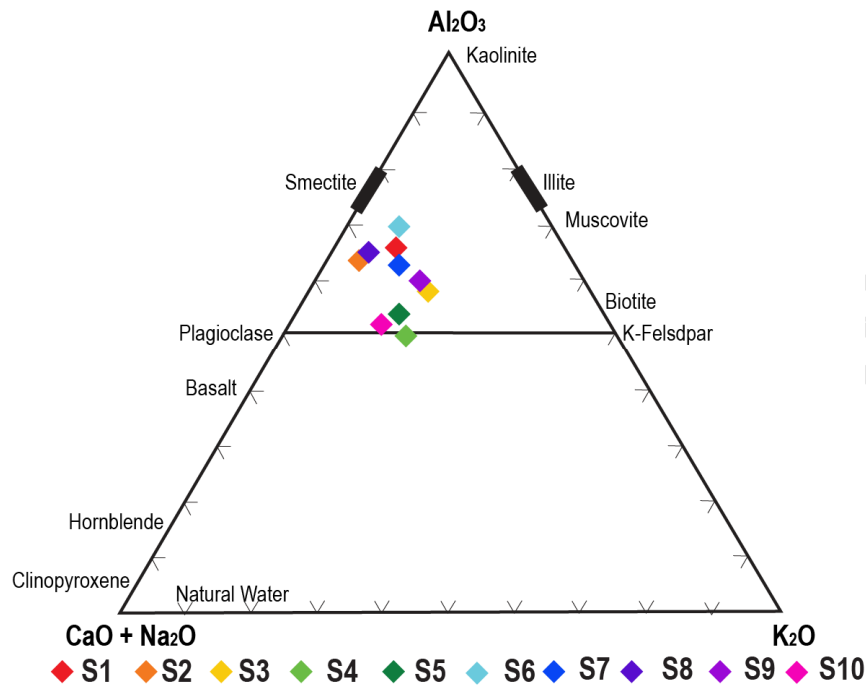
479 [2]Total reported on an LOI basis

480 [3]LOI: loss on ignition (% weight loss in air at 950°C for 1 hour)

481 [4]Ferrous and ferric iron determined by wet chemistry

482 *Reported in ppm (all others in weight percent)

483

484

485

486

Figure 7. A-CN-K diagram showing the weathering trend and composition of the 10 samples

(Nesbitt and Young, 1984).

489

3.3.2 Laser-Induced Breakdown Spectroscopy (LIBS)

The LIBS dataset provides information on the presence and relative abundance of major and

trace elements across three wavelength ranges (UV, violet, visble). The elements identified in the

UV range are Fe, Si, Mg, Al, Ca and Ti; in the blue and in the violet range are Si, Mg, Al, Ca,

and Zr; and in the visible range are Si, Mg, Ca, and Na (Figure 8). There is variability between

samples in terms of the peak height for different elements indicating changes in the abundance.

The most striking are the Ca peaks in the UV spectrum (Figure 8A). However, this is not the case

in all three wavelength ranges and does not necessarily correspond to high Ca concentrations as

quantification and relative concentrations requires instrument calibration using standards (Figure

8C).

500

501
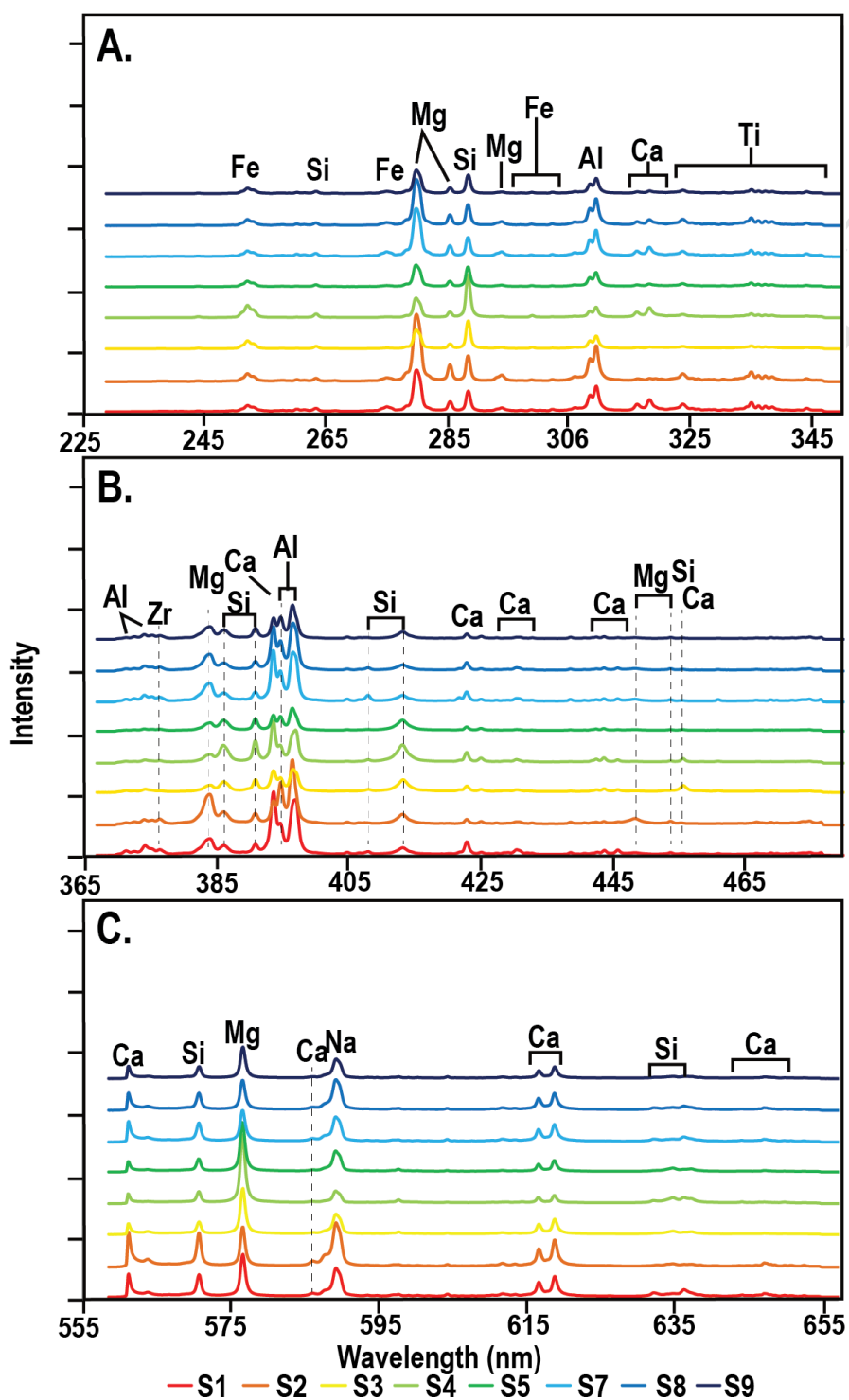
Figure 8. LIBS Spectra for 9 of the 10 samples. A. Spectra in the UV wavelength (225-350 nm)

B. Spectra in the blue and violet wavelength range (365-480 nm) C. Spectra in the visible

wavelength (555-657 nm).

505

506   *3.4. Raman Spectroscopy*

507   *3.4.1 532 nm Raman*

508   Raman spectra were collected from both powdered and whole rock samples and are

509   characterized by a large fluorescence feature indicative of iron centered at either ~1800 or

510   ~2000-2200 cm^{-1}. Representative spectra are presented in Figure 9. Peaks of single data point

511   width are the result of "hot pixels" in the detector and as artifacts of the analysis are not be

512   discussed further.

513

514   Multiple (2-6) spectra were collected for each sample (both surface and powdered), and the

515   Raman bands observed in each sample vary in position and strength. In some cases, such as S1

516   there are no discernable Raman bands, likely due to the high fluorescence signal which is a

517   limitation with using a 532 nm source. Samples S3 and S4 are unique in that their spectra also

518   have a prominent fluorescence feature at ~3400 cm^{-1} which is characteristic of chlorophyll.

519   Spectra from all samples except S1 have a 467 cm^{-1} Raman band associated with quartz. Calcite

520   (1083 cm^{-1}) and gypsum (1007 cm^{-1}) bands are observed in multiple samples as weak bands

521   (Table 4). There are also several bands located in the 1000-1600 cm^{-1} range which are

522   characteristic of organic carbon, the strongest of which is seen in sample S2 at 1069 cm^{-1}. The

523   organic carbon peaks in samples S3 and S4 at 1156 cm^{-1} and 1511 cm^{-1} are likely the result of β-

524   carotene (Edwards et al., 2005; Rhind et al., 2014). Table 4 summarizes the Raman bands

525   observed in each sample and the complete dataset is included in the supplementary text.

526

527

528

529   **Table 4.** Summary of the Raman bands (cm^{-1}) observed in each sample and the minerals

530   assigned to them.

ID	Surface	Powder
BC4-S1	-	-
BC4-S2	-	Quartz (467), Calcite (1083), Organic Carbon (1069)
BC4-S3	Quartz (467), Gypsum (1007),β-Carotene (1156, 1511) Chlorophyll (~3400)	Quartz (467), Gypsum (1007), β-Carotene (1156, 1511) Chlorophyll (~3400)

BC4-S4	Quartz (467), Gypsum (1007), Organic Carbon (1156, 1511), Chlorophyll (~3400)	Quartz (467), Organic Carbon and β-Carotene (1069, 1156, 1390 1511) Chlorophyll (~3400)
BC4-S5	Quartz (467), (653?)	Quartz (467)
BC4-S6	Quartz (467)	Quartz (467)
BC4-S7	-	Quartz (467)
BC4-S8	-	Quartz (467)
BC4-S9	Quartz (467)	Quartz (467), Anatase? (397,518,640)
BC4-S10	-	Gypsum (1007)

531

532

533
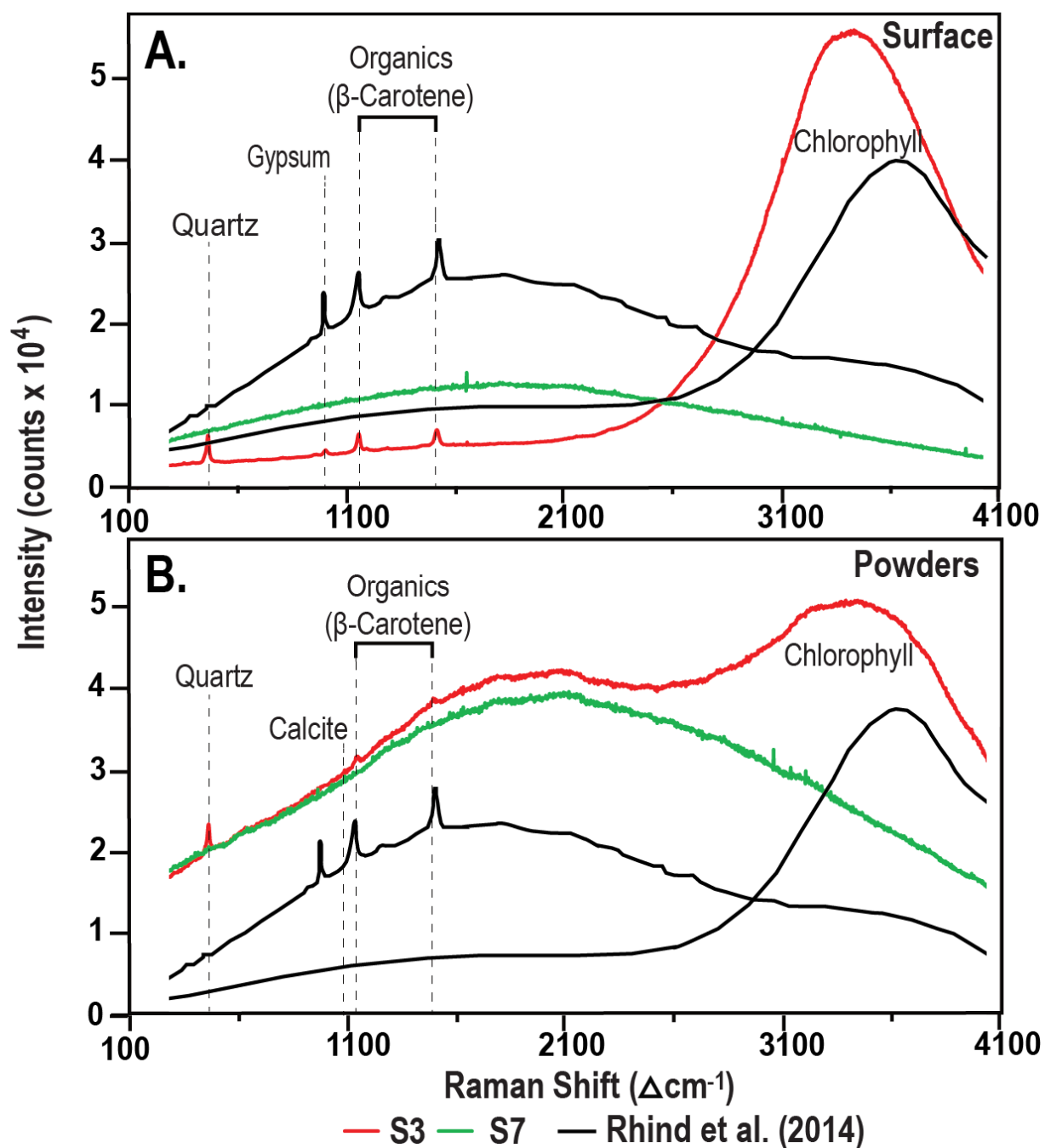
Figure 9. Raman (532 nm excitation) spectra of samples S3, and 7 are dominated by a fluorescence hump, a likely result of iron. Data from Rhind et al. (2014) is plotted to show the characteristic Raman features associated with beta-Carotene, chlorophyll and gypsum.

3.4.2 Time Resolved Raman Spectroscopy

541 The Raman spectra of the 10 samples is dominated by strong short-lived luminescence (<40 ns)

542 indicating the presence of organic carbon, with samples S2 and S4 exhibiting the strongest

543 luminescence (Figure 10). Weak Raman lines of α-quartz (464 cm^{-1}) are superimposed on the

544 luminescence background in samples S3 and S5 samples. Atmospheric O_2 (1554 cm^{-1}) and N_2

545 (2331 cm^{-1}) lines are observed in the spectra of all the samples.

546

547
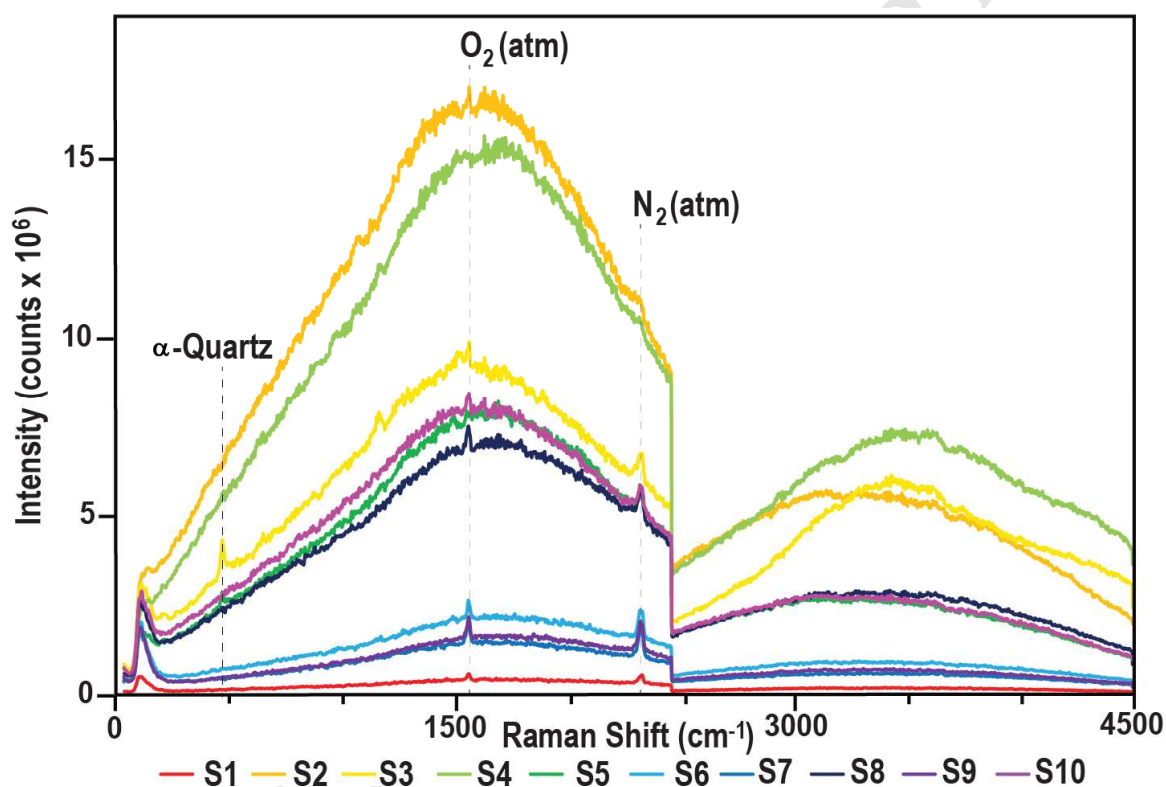
548
549 **Figure 10.** Time resolved Raman spectra of the 10 samples are dominated by short lived

550 luminescence and atmospheric O_2 and N_2.

551

552

553 *3.4.3 UV Raman*

554

555 The features observed in the UV Raman spectra are summarized in Table 5. The signal to noise

556 ratio for several of the samples (S1, S2, S9) was poor to allow for peak identification. The

557 spectra of all the samples are dominated by peaks characteristic of organic compounds (Table 5,

558 Figure 11). In most cases, the peak at ~2350 cm^{-1} is most prominent (e.g., Figure 11B). Minor

559 mineral phases detected include quartz, and features associated with sulphates, phosphate and

560 oxide minerals (Figure 11). The complete dataset is included in the Supplementary Materials.

561

562 **Table 5.** Summary of the Raman bands (cm^{-1}) observed in each sample and the compounds and

563 minerals assigned to them.

Sample ID	Raman Signal (cm^{-1})
BC4-S1	Poor SNR
BC4-S2	Poor SNR
BC4-S3	Organic Carbon, Quartz (460-465), Sulfates, Phosphate (987)
BC4-S4	Organic Carbon
BC4-S5	Organic Carbon, Sulfate
BC4-S6	Organic Carbon, Sulfate
BC4-S7	Organic Carbon, Oxide? (668)
BC4-S8	Organic Carbon, Sulfate, Oxides (Cr or Fe) (560, 620-668)
BC4-S9	Poor SNR
BC4-S10	Organic Carbon

564 *Organic peaks at ~1500, 2350, 2600-2700, C-C vibration (1315, 1550), C=O stretching of
565 complex esters (~1730), NH-CH or NH3- (~2320-30)
566 *Sulfate peaks at ~980 and 1100 cm-1
567
568
569

570

571
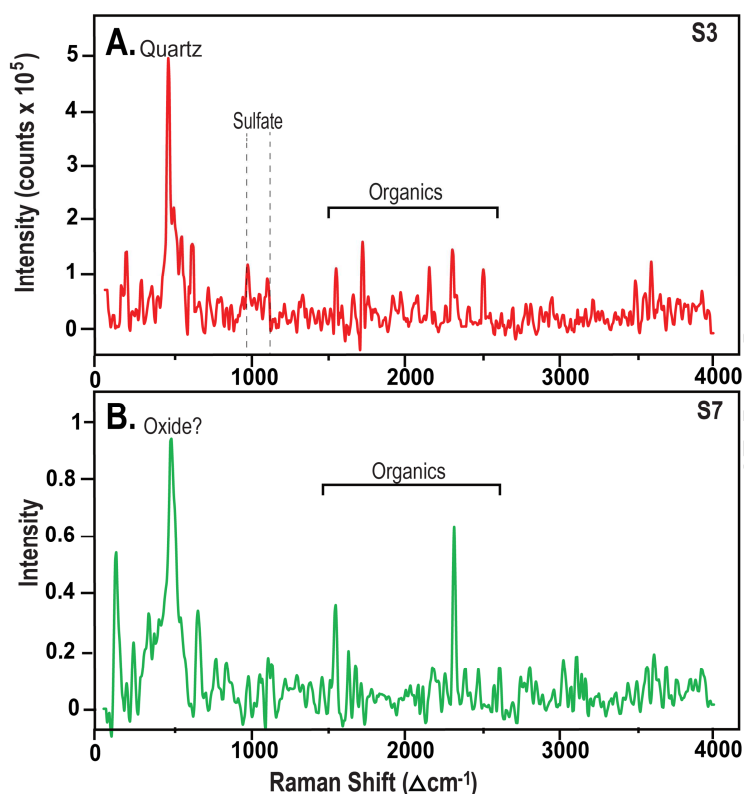
Figure 11. UV-Raman spectra of samples -S3 and S7. There are multiple bands indicative of
organic carbon at 1550 cm^{-1} (C-C), ~1730 cm^{-1} (C=O), ~2320-30 (NH-CH or NH$_3$), and 2600-
2700 cm^{-1}.

575

576

4.0 Discussion

578

4.1 Mineralogical Context

Mars has a diverse surface mineralogy, with well over 100 mineral species detected to date (e.g.,
Ehlmann and Edwards, 2014). The detection of hydrated, evaporite, and hydrothermal minerals
as well as trace metal enrichments has important implications for astrobiology in terms of
habitability, biosignature preservation, and as potential biosignatures (Anderson et al., 2017;
Brolly et al., 2017; Camara et al., 2016; Domagal- Goldman et al., 2017; Desquire et al., 2017;
Gasda et al., 2017; Kosek et al., Rull et al., 2017). This includes minerals such as gypsum and
calcite as well as their constituents and other elements common in evaporite deposits including
Ca, Na, K, Sr. The other suite of astrobiologically relevant elements discussed are the "essential"

588 micro and macro nutrients"; including S, N, P, Cu, Zn, Ni, Mn (McKay, 2014). While the

589 samples are dominated by quartz, which is not a major component of the Martian crust (Ehlmann

590 and Edwards, 2014), the geomorphology and history of water in the region has resulted in the

591 presence of several astrobiologically relevant minerals which were detected using multiple

592 techniques, including calcite, gypsum, and montmorillonite.

593

594 In terms of number and diversity of mineral phases detected with a single instrument, X-ray

595 diffraction (MSL CheMin) is shown to be the most effective single method and provides the

596 opportunity for quantitative mineralogy. However, the same results can be inferred by the

597 combined use of the reflectance and Raman spectral datasets which in several cases identified

598 minerals which were not identified in the XRD data such as trace carbonates down to <1 wt%

599 (Figure 6). While quantification is more complex with these datasets, the characterization of

600 mineral species and chemistry is possible from spectral data. The XRD patterns of the Hanksville

601 samples are dominated by quartz and a clay phase (nontronite and/or montmorillonite), which is

602 difficult to identify in XRD, but is readily detected in the VNIR-SWIR datasets, and in most

603 cases is likely montmorillonite. In addition to characterizing the phyllosilicate phases in the

604 samples, reflectance spectroscopy can also provide information on sample chemistry based on

605 the relative position of the metal-OH, Al-OH and iron absorption features. Clay minerals are

606 critically important for organic preservation in alluvial environments (Hays et al., 2017). Raman

607 spectroscopy detected quartz and in some cases also sulfates and calcite but did not provide

608 meaningful information on the clay content of the samples

609

610 Reflectance spectroscopy also effectively identified carbonate and sulfate phases, both of which

611 are important for paleoconditions/habitability (evaporite deposits) and whose formation can be

612 biologically mediated, producing spectral differences (e.g., Ronholm et al, 2013, 2014; Berg et

613 al., 2014; Korbalev et al., 2017). Evaporitic phases such as gypsum and calcite are also of

614 astrobiological relevance in the context of habitability and preservation of organic biomarkers

615 (e.g, Baque et al., 2016; Stromberg et al., 2014). Carbonate was detected in the UV-Vis-NIR and

616 FTIR spectra of samples S1,3,4,5,9,10, and gypsum was detected in the UV-Vis-NIR spectra of

617 samples S10 (S3,4,9 in 532nm Raman). The presence of these phases is easier to distinguish in

618   both reflectance spectra and Raman spectra than in the XRD data when the occur in minor or

619   trace amounts in the samples (<1%).

620

621   In terms of detection of major and minor to trace elements (e.g., Zr, Ti) the Hanksville samples

622   show that LIBS and XRF are roughly comparable, however, this is a qualitative measure. An

623   important feature of LIBS is that is very effective at detecting light elements such as C, Li, S,

624   Mg, Na and Ca (e.g., Harmon, Russo and Hark, 2013; Hark and Harmon, 2014) as well as

625   heavier elements such as Sr and Rb in geologic materials, although this is not reflected in our

626   dataset due to the experimental setup. This is important as XRF has limited capability with the

627   light elements and cannot detect C. It should also be noted that lab base XRF is not necessarily

628   the best proxy for the PIXL instrument as it is a bulk measurement whereas PIXL, like LIBS, is a

629   point measurement on an in situ sample. However, it provides a useful baseline for which

630   elements may be detectable by the PIXL instrument, which will also have the benefit of spatially

631   resolved geochemical data. The UV-Vis-NIR datasets provide evidence for Fe^{3+}/Fe^{2+} redox

632   couples what are important in an astrobiological context. However, iron that is observed in the

633   surface sensitive spectral data (Raman fluorescence feature, UV-Vis-NIR crystal field

634   transitions) does not necessarily reflect the total iron content or mineralogy of the samples

635   identified by and XRF or XRD. It is in many cases the result of surface weathering, which is

636   easily observed in the color of the samples. This is important when working with iron stained

637   samples and something that may be used to when considering sample selection and which

638   techniques to use for sample characterization. In the case of the Hanksville samples, it was clear

639   from the sample surface if this would be an issue. For example, sample S7 which is reddish has

640   enhanced Fe features in the UV-VIS region of the spectrum (Figure 5) and high fluorescence in

641   the Raman data (Figure 9). This highlights the importance of selecting the correct technique for

642   characterization, and can be mitigated with the application of LIBS analysis which is capable of

643   penetrating this iron stained layer for geochemical depth profiling.

644

645   *4.3 Organic Biosignature Detection*

646   One of the primary objectives of the MSRAD sampling strategy was the collection of samples

647   with high organic carbon content, and the overall low TOC of the rover track samples is low

648   (<0.02%) by terrestrial standards. However, this provides a unique opportunity to assess the

649 capability of techniques employed by flight instrumentation such as Raman spectroscopy, and

650 reflectance spectroscopy for detecting organic molecules. This is increasingly important as

651 upcoming missions are focused on the search for past and present like (e.g., Mars2020, EcoMars)

652 where the primary objective is the direct detection of biosignatures, with organic molecules

653 being an important target (Grotzinger, 2014; Domagal-Goldman and Wright, 2016; Rull et al.,

654 2017). This objective has driven the development of a number of new flight instruments with

655 analytical capabilities for the detection of organic molecules by LIBS and Raman (e.g,

656 SuperCam, SHERLOC, RSL) (Jessberger et al., 2003; Skulinova et al., 2014; Eshelman et al,

657 2015; Dequiare et al., 2016; Laing et al., 2016.; Rull et al., 2017). While our LIBS experimental

658 setup was not optimized for C detection, the detection limits for C in samples with <0.5%

659 organic carbon have not been well established (Dequire et al., 2017), so it is unlikely that LIBS

660 data could have provided definitive C detection in most or any of the rover track samples.

661

662 Organic carbon was detected in multiple samples by both Raman and reflectance spectroscopy

663 (proxies for Mars2020 SuperCam, Exomars RLS and Mastcam instrumentation) and the results

664 are summarized in Table 6. The most prominent and conclusive organic biosignature observed is

665 the presence of chlorophyll and carotene detected in the UV-VIS-NIR and Raman spectra in

666 samples S3 and S4 (Figure 4,5,9). The detection and characterization of organic compounds in

667 the UV-VIS-NIR and IR range of the spectra has been widely applied in the context of

668 astrobiology (e.g., Preston et al., 2011; Izawa et al., 2014; Preston et al., 2015). However, apart

669 from the carotene and chlorophyll absorption features below ~800 nm, there are no other

670 indications of organic compounds observed in the reflectance spectra of any of the samples.

671 While this most likely evidence of present endolithic life, the detection of such molecules may

672 have implications for Mars as they have been shown to be somewhat stable under Martian

673 surface conditions (e.g., Baque et al., 2016; Stromberg et al., 2014). However, this stability and

674 preservation potential is dependent on their endolithic habitat, and so detection requires a fresh

675 surface exposed by abrasion (e.g., RAT (rock abrasion tool)) or sample crushing (Baque et al.,

676 2016; Stromberg et al., 2014). Sample S4 is a piece of sandstone and S3 is unconsolidated white

677 clay material, and while the chlorophyll and carotene were detected in both surface and crushed

678 samples, it is likely that the surface sampled was a fresh surface which was exposed during

679 sample collection and transport.

680

681 The Raman measurements (532 nm, TR, UV) collected on the Hanksville samples all detected

682 organic carbon with variable success in multiple samples. While the Hanksville samples all have

683 TOC values of <0.07% with most below 0.03%, Raman spectroscopy has emerged as a powerful

684 technique for the characterization and detection of low concentration organic compounds

685 (Mars2020 SuperCam and SHERLOC, ExoMars RLS) (e.g., Skulinove et al, 2014; Cloutis et al.,

686 2016, Eshelman and Edwards, 2014; Eshelman et al., 2015; Laing et al., 2016; Abbey et al.,

687 2017). The detection of ~0.04 wt % condensed carbon has been reported in simulate Martian

688 regolith samples by UV-Raman (Abbey et al., 2017), and Raman spectroscopy is capable of

689 distinguishing between PAH compounds (Cloutis et al., 2016). The 532 nm Raman spectrum are

690 dominated by fluorescence feature (likely iron) and like the reflectance data were most

691 successful at detecting chlorophyll and carotenes in samples S3 and S4. However, this dataset

692 only detected carbon compounds in one other sample (S2), the highest ranked sample taken by

693 the rover based on potential for organic content carbon. This sample was ranked highly due to its

694 greenish color and fine-grained nature which was hypothesized to be the result of high clay

695 content and potential iron redox gradients (Caudill et al., 2019a). High clay content is reflected in

696 the XRD and the reflectance spectral results, and the sample also had the highest Al_2O_3 and

697 nitrogen contents, and elevated S values.

698

699 Sample S2 has the highest organic luminescence in the time resolved Raman spectra, followed

700 by the chlorophyll and carotene containing samples (S3 and S4). Short lived fluorescence in

701 itself has been proposed as a possible biosignature (Eshelman et al., 2015). All of the samples

702 except S1 exhibit some degree of short-lived luminescence (Figure 10), the magnitude of which

703 roughly reflects the reported TOC values (Table 3). This is significant given that the TOC of

704 several samples was <0.01% but they still show minor short-lived luminescence. UV-Raman

705 also detected organic carbon in all samples where the SNR allowed for peak identification. All

706 the samples suffer from low SNR which makes compound specific identification difficult.

707 Despite this, the results highlight the exceptionally low detection limits of UV-Raman for

708 organic compounds and begins to explore the breadth of information that can be extracted from

709 UV-Raman datasets. This approximates the data from the Mars2020 SHERLOC instrument

710 which has the potential to identify reduced carbon compounds but may not provide sufficient

711 structural information to distinguish between a biological signal and extraterrestrial organic input
712 (Hays et al., 2017).
713

714 *4.3 Paleohydrological Context*
715 The ten samples in this study showed substantial variance in their overall low carbon content
716 (<0.07% TOC). Work on terrestrial contemporary fluvial systems has shown that locations or
717 periods where fluvial channels intersect geologic boundaries or are introduced to larger stream
718 networks (representing the potential of a particular nutrient or resource delivery to an area in
719 which is it biologically limiting) are typically more biogeochemically active, driven by
720 hydrology (McClain et al., 2003; Krause et al., 2017). Thus the variance in organic or carbon
721 content, or other biosignature detection (such as chlorophyll detection through spectroscopy)
722 may be attributable to either variations in flow through time or space at the site (Williams et al.,
723 2009). All of these samples with the exception of S4 were *in situ* unconsolidated surficial
724 material some of which can be directly correlated to rover traverse samples. Future knowledge of
725 Martian geologies and paleoflows may be linked to known limiting resources or nutrients for
726 biological production which may have resulted in biosignature production and preservation.
727 Future terrestrial field campaigns may continue to test this hypothesis by sampling for detectable
728 biosignatures along transects of geologic units which were linked through apparent
729 paleohydrologic networks to determine the applicability of this approach for designing sampling
730 campaigns for future Martian missions.
731
732

733 **Table 6.** Summary of the biosignatures and astrobiologically relevant minerals and elements
734 detected and *detectable* by each technique.

Technique	Organic Material	Organic Biosignatures	Minerals or Elements
LIBS	-	-	Na, Ca, (*Mn, H, B, C, K, Sr, Rb)*
Raman	S2, S3, S4	S3, S4	Gypsum, Calcite
Time Resolved Raman	All samples	-	-
UV-Vis-NIR Spectroscopy	S3, S4	S3, S4	Gypsum, Carbonates, Clays
FTIR	-	-	Sulfates, Carbonates,

Spectroscopy			Clays
XRF	-	-	K, Na, P, S, Sr, Mn
UV Raman*	S3,4,5,6,7,8,10	-	Sulfates, OH-
XRD	-	-	Gypsum, Calcite, Clays
Mass Spectrometry	S1,2,3,4,6,7,8,10, (TOC)	-	C, N, S, TOC

*poor SNR for samples S1,S2,S9

735

736

737
738 **6. Conclusions**

739

740 The search for extant life on Mars hinges in the ability to detect biosignatures using rover

741 mounted instruments. But equally important is identifying regions where organic biosignatures

742 may have formed and been preserved using regional scale paleohydrological models as well as

743 mineralogical and geochemical datasets. While the organic carbon content of the Hanskville 10

744 samples was overall low in a terrestrial context, complex organic carbon molecules were

745 detected using multiple rover equivalent instruments and these values are not low in the context

746 of Mars (Ming et al., 2014; Freissinet et al., 2015). The mineralogy of the Hanksville samples is

747 dominated by quartz, but astrobiologically relevant hydrated and evaporite minerals were

748 detected by multiple techniques which can be used to guide site selection for further analysis.

749 The geochemistry of the samples also points towards the presence of undetected trace mineral

750 phases detectable by LIBS and XRF (e.g, Ti and Zr) which may be relevant for redox and

751 paleoenvironmental context.

752

753 In addressing the CanMars MSRAD goal of selecting samples with organic carbon and

754 biosignatures, organic carbon was detected in the top 2 ranked samples (S2- Neils, and S7-

755 Astrid) using Raman (UV, 532 nm and time resolved) and reflectance spectroscopy (UV-Vis-

756 NIR). Sample S2 proved to be the most promising target for further analysis (e.g., GC-MS) and

757 potential sample return given the elevated N and S values and high clay contents. However, to

758 reach any such conclusions on sample relevance requires the evaluation of at least one of the

759 Raman datasets (UV-in this case) as well as spectral data. Relying only on TOC presence or

760 abundance is insufficient as in this case, the highest TOC values were extracted from the sample

761 has the least astrobiological significance in terms of mineralogy and geochemistry (S4) as it a

762 sandstone boulder dominated by quartz (94.89% SiO_2). This highlights the importance of using

763 multiple techniques to characterize sample context. Organic biomarkers (chlorophyll and

764 carotene) were detected in samples S3 and S4 by reflectance and Raman (532 nm) spectroscopy.

765 The organic carbon content of the samples is below the detection limits of FTIR spectroscopy

766 and LIBS but can be readily detected with Raman spectroscopy. The UV-Raman (Mars2020

767 SHERLOC) data provided the greatest insights into the potential structure of the organic carbon.

768

769 The importance of using multiple datasets for characterizing sample mineralogy and providing

770 context for any detected organic compounds is highlighted in these results. UV and time-

771 resolved Raman are shown to be the most effective instrument for detection of organic

772 molecules, however, both provided little mineralogical context, and compound identification was

773 not possible. By comparing mineralogical, spectral, and geochemical datasets it is clear that the

774 sample with the highest TOC values and strongest organic carbon signature may not be the most

775 relevant. While XRD provided the greatest breadth of mineral detection (major and trace), the

776 same mineralogy can be determined from the Raman and reflectance spectral results with

777 elemental data (LIBS, XRF) guiding trace mineral inferences. Reflectance spectroscopy provides

778 the greatest compound specific information (chorophyll) in this sample suite, but in the context

779 of Mars, its strengths lie in mineralogical detection and characterization which is reflected in the

780 ubiquity of spectrometers on planetary mission payloads.

781

782

791

792

793 **References**

794

795 Abbey,S.,1983. Studies in "Standard Samples" of silicate rocks minerals 1962–1982. Geological

796 Survey of Canada Paper, pp. 83–115.

797

798 Abbey, W.J., Bhartia, R., Beegle, L.W., DeFlores, L., Paez, V., Sijapati, K., Sijapati, S.,

799 Williford, K., Tuite, M., Hug, W. and Reid, R., 2017. Deep UV Raman spectroscopy for

800 planetary exploration: The search for in situ organics. Icarus, 290, pp.201-214.

801

802 Anderson, D.E., Ehlmann, B.L., Forni, O., Clegg, S.M., Cousin, A., Thomas, N.H., Lasue, J.,

803 Delapp, D.M., McInroy, R.E., Gasnault, O., Dyar, M.D., Schröder, S., Maurice, S., and Wiens,

804 R.C. 2017. Characterization of Laser-Induced Breakdown Spectroscopy (LIBS) emission lines

805 for the identification of chlorides, carbonates, and sulfates in salt/basalt mixtures for the

806 application to MSL ChemCam data. J. Geophys. Res. Planets.

807

808 Battler, M.M., Clarke, J.D.A., Coniglio, M., 2006. Possible analogue sedimentary and

809 diagenetic features for Meridiani Planum sediments near Hanksville, Utah: implications for

810 Martian Field studies. Mars Analog Res. Am. Astronaut. Soc. Sci. Technol. Ser. Spec. Publ. 111,

811 55–70.

812

813 Blanco, Y., Gallardo-Carreno, I., Ruiz-Bermejo, M., Puente-Sánchez, F., Cavalcante-Silva, E.,

814 Quesada, A., Prieto-Ballesteros, O. and Parro, V., 2017. Critical Assessment of Analytical

815 Techniques in the Search for Biomarkers on Mars: A Mummified Microbial Mat from Antarctica

816 as a Best-Case Scenario. Astrobiology, 17(10), pp.984-996.

817

818 Baqué, M., Verseux, C., Böttger, U., Rabbow, E., de Vera, J.P.P. and Billi, D., 2016.

819 Preservation of biomarkers from cyanobacteria mixed with Marslike regolith under simulated

820 Martian atmosphere and UV flux. Origins of Life and Evolution of Biospheres, 46(2-3), pp.289-

821 310.

822

823 Beaty, D.W., Hipkin, V., Caudill, C., Hansen, R., Hausrath, E., Maggiori, C., McCoubrey, R.,
824 Parrish, J., Ralston, S., 2019. Geological Evaluation of the MSRAD Field Site by a Human Field
825 Party: Implication for Rover Based Exploration Operations and for the Future Human
826 Exploration of Mars. Planetary and Space Science (this issue).
827
828 Berg, B.L., J. Ronholm, D.M. Applin, P. Mann, M. Izawa, E.A. Cloutis, and L.G. Whyte, 2014.
829 Spectral features of biogenic calcium carbonates and implications for astrobiology. International
830 Journal of Astrobiology, 13, 353-365.
831
832 Balme, M., Grindrod, P., Sefton-Nash, E., Davis, J., Gupta, S., Fawdon, P., Sidiropolous, P.,
833 Yershov, V., Muller , J-P., 2015. Aram Dorsum: A Noachian Inverted Flivial Channel system
834 and Candidate ExoMars 2018 Rover Landing Site. LPSC, 45, Abstract #1321
835
836 Brolly, C., Parnell, J., & Bowden, S., 2017.. Raman spectroscopy of shocked gypsum from a
837 meteorite impact crater. International Journal of Astrobiology, 16(3), 286-292.
838
839 Buzgar, N., Apopei, A.I., 2009. The Raman study on certain carbonates. Analele Stiint. ale Univ.
840 "Al. I. Cuza" - Iasi 55, 97–112.
841
842 Buzgar, N., Buzatu, A., Sanislav, I. V., 2009. The Raman study on certain sulfates. Analele
843 Stiint. ale Univ. "Al. I. Cuza" 55, 5–23.
844
845 Cámara, B., Souza-Egipsy, V., Ascaso, C., Artieda, O., De Los Ríos, A., & Wierzchos, J. 2016.
846 Biosignatures and microbial fossils in endolithic microbial communities colonizing Ca-sulfate
847 crusts in the Atacama Desert. Chemical Geology, 443, 22-31.
848
849 Caudill, C.M., Pontefract, A. Osinski, G., Tornabene, L., Xie, T., Mittelholz, A., Poitras, J.,,
850 Simpson, S., Svensson M., Grau, A., Godin, E., Pilles, E., Francis, R., Williford, D., Tuite, M.,
851 Battler, M., Hipkin, V., Haltigan., T., the 2015 & 2016 Science Team Members. 2019a. CanMars
852 Mission Science Results and Review of Optimization for Sample Selection for Mars Samples
853 Return (MSR) based Science Operations and Procedures. Planetary and Space Science (this
854 issue)
855

856   Caudill, C.M., Osinski, G., Pilles E., Sapers, H.M., Pontefract, A.J., Duff, S., Laughton, J.,

857   O'Callaghan, J., Sopoco, R., Tolometti, G., Tuite, M., Williford, K.H., Xie, Tianqi., 2019b.,

858   Field and laboratory validation of the science team findings from the CanMars rover analogue

859   mission. Planetary and Space Science (this issue).

860

861   Chen, Y., Zhou, Y., Zhang, L., Wu, M., Yan, S., 2007. Discovery of CH4-rich high-pressure

862   fluid inclusions hosted in analcime from Dongying depression, China. J. Pet. Sci. Eng. 56, 311–

863   314. doi:http://dx.doi.org/10.1016/j.petrol.2006.10.005

864

865   Chio, C.H., Sharma, S.K., Muenow, D.W., 2005. Micro-Raman studies of hydrous ferrous

866   sulfates and jarosites. Spectrochim. Acta Part A Mol. Biomol. Spectrosc. 61, 2428–2433.

867   doi:http://dx.doi.org/10.1016/j.saa.2005.02.021

868

869   Clarke, J. D. A. and Pain, C. F. 2004. From Utah to Mars: regolith-landform mapping and its

870   application. In Cockell, C. C. (ed.) Mars Expedition Planning. American Astronautical Society

871   Science and Technology Series, 107, pp. 131-160

872

873   Clarke, J.D. and Stoker, C.R., 2011. Concretions in exhumed and inverted channels near

874   Hanksville Utah: implications for Mars. International Journal of Astrobiology, 10(3), pp.161-

875   175.

876

877   Cloutis, E.A., Mann, P., Izawa, M.R.M., Applin, D., Samson, C., Kruzelecky, R., Glotch, T.D.,

878   Mertzman, S.A., Mertzman, K.R., Haltigan, T.W., Fry, C., 2015. The Canadian space agency

879   planetary analogue materials suite. Planetary and Space Science. 119, pp.155-172.

880

881   Cloutis, E. A., Szymanski, P., Applin, D., Goltz, D., 2016. Identification and discrimination of

882   polycycluc aromatic hydrocarbons using Raman spectroscopy. Icarus, 273, 211-230.

883

884   Daly, M., 2015. Science Definition Study for an Ultraviolet Raman Spectrometer for the

885   Identification of Organic Carbon on Mars.

886

887 Dequaire, T., P.Y. Meslin, M. Jaber, W. Rapin, A. Cousin, O. Gasnault, P. Beck, O. Fourni, E.

888 Cloutis, S. Maurice, D. Applin, J.R. Johnson, N. Mangold, C. Szopa, P. Coll, and the MSL

889 Science Team., 2016. Search for organic matter at Mars with LIBS and reflectance

890 complementary measurements of the ChemCam instruments onboard the Curiosity rover. Lunar

891 and Planetary Science Conference, 47, abstract #1364.

892

893 Domagal-Goldman, S.D. and K.E. Wright et al., 2016. The Astrobiology Primer v2.0.

894 Astrobiology, 16, 8, 561-653.

895

896 Downs, B., Robinson, S., Yang, H., Mooney, P., 2015. RRUFF Project. Dep. Geosci. Univ.

897 Arizona.

898

899 Edwards, H.G., Moody, C.D., Villar, S.E.J. and Wynn-Williams, D.D., 2005. Raman

900 spectroscopic detection of key biomarkers of cyanobacteria and lichen symbiosis in extreme

901 Antarctic habitats: evaluation for Mars Lander missions. *Icarus*, *174*(2), pp.560-571.

902

903 Ehlmann, B.L., and C.S. Edwards. 2014. Mineralogy of the Martian surface. Annual reviews in

904 Earth and Planetary Science, 42, 291-315.

905

906 Ehrenfreund, P., Röling, W.F.M., Thiel, C.S., Quinn, R., Sephton, M.A., Stoker, C., Kotler, J.M.,

907 Direito, S.O.L., Martins, Z., Orzechowska, G.E. and Kidd, R.D., 2011. Astrobiology and

908 habitability studies in preparation for future Mars missions: trends from investigating minerals,

909 organics and biota. International Journal of Astrobiology, 10(3), pp.239-253.

910

911 Ehlmann, B.L., and C.S. Edwards (2014) Mineralogy of the Martian surface. Annual reviews in

912 Earth and Planetary Science, 42, 291-315.

913

914 Eshelman, E., Daly, M. G., Slater, G., Dietrich, P., & Gravel, J. F. (2014). An ultraviolet Raman

915 wavelength for the in-situ analysis of organic compounds relevant to astrobiology. Planetary and

916 Space Science, 93, 65-70.

917

918   Eshelman, E., M.G. Daly, G. Slater, and E. Cloutis, 2015. Time-resolved detection of aromatic

919   compounds on planetary surfaces by ultraviolet laser induced fluorescence and Raman

920   spectroscopy. Planetary and Space Science, 119, 200-207.

921

922   Farley, K. A., and K. H. Williford, 2017, Seeking signs of life, and more: NASA's Mars 2020

923   mission, Eos, 98, https://doi.org/10.1029/2017EO066153. Published on 11 January 2017.

924

925   Freissinet, C., Glavin, D.P., Mahaffy, P.R., Miller, K.E., Eigenbrode, J.L., Summons, R.E.,

926   Brunner, A.E., Buch, A., Szopa, C., Archer, P.D. and Franz, H.B., 2015. Organic molecules in

927   the sheepbed mudstone, gale crater, mars. Journal of Geophysical Research: Planets, 120(3),

928   pp.495-514.

929

930   Freeman, J.J., Wang, A., Kuebler, K.E., Jolliff, B.L., Haskin, L.A., 2008. Characterization of

931   natural feldspars by raman spectroscopy for future planetary exploration. Can. Mineral. 46,

932   1477–1500. doi:10.3749/canmin.46.6.1477

933

934   Frost, R.L., Fredericks, P.M., Kloprogge, J.T., Hope, G.A., 2001. Raman spectroscopy of

935   kaolinites using different excitation wavelengths. J. Raman Spectrosc. 32, 657–663.

936   doi:10.1002/jrs.722

937

938   Frost, R.L., López, A., Theiss, F.L., Romano, A.W., Scholz, R., 2014. A vibrational

939   spectroscopic study of the silicate mineral analcime – $Na_2(Al_4SiO_4O_{12})\cdot 2H_2O$ – A natural

940   zeolite. Spectrochim. Acta Part A Mol. Biomol. Spectrosc. 133, 521–525.

941

942   Gainey, S.R., Hausrath, E.M., Adcock, C.T., Tschauner, O., Hurowitz, J.A., Ehlmann, B.L.,

943   Xiao, Y. and Bartlett, C.L., 2017. Clay mineral formation under oxidized conditions and

944   implications for paleoenvironments and organic preservation on Mars. Nature

945   Communications, 8(1), p.1230.

946

947   Gasda, P.J., E.B. Haldeman, R.C. Wiens, W. Rapin, T.F. Bristow, J.C. Bridges, S.P. Schwenzer,

948   B. Clark, K. Herkenhoff, J. Frydevang, N.L. Lanza, S. Maurice, S. Clegg, D.M. Delapp, V.L.

949 Sanford, M.R. Bodine, and R. McInroy, 2017. In situ detection of boron by ChemCam in Mars.

950 Geophysical Research Letters, 44, 17, 8739-8748.

951

952 Grotzinger, J.P., 2014. Habitability, taphonomy, and the search for organic carbon on Mars.

953 Science, 343, 386-387.

954

955 Haley, L. V, Wylie, I.W., Koningstein, J.A., 1982. An investigation of the lattice and interlayer

956 water vibrational spectral regions of muscovite and vermiculite using Raman microscopy. A

957 Raman microscopic study of layer silicates. J. Raman Spectrosc. 13, 203–205.

958 doi:10.1002/jrs.1250130217

959

960 Harmon, R.S., Russo, R.E., Hark, R.R., 2013. Applications of laser-induced breakdown

961 spectroscopy for geochemical and environmental analysis: A comprehensive review.

962 Spectrochimica Acta Part B: Atomic Spectroscopy, 87, 11-26.

963

964 Hark, R.R. and Harmon, R.S., 2014. Geochemical fingerprinting using LIBS. In *Laser-Induced*

965 *Breakdown Spectroscopy* (pp. 309-348). Springer, Berlin, Heidelberg.

966

967 Hays, L.E., Graham, H.V., Des Marais, D.J., Hausrath, E.M., Horgan, B., McCollom, T.M.,

968 Parenteau, M.N., Potter-McIntyre, S.L., Williams, A.J. and Lynch, K.L., 2017. Biosignature

969 preservation and detection in Mars analog environments. Astrobiology, 17(4), pp.363-400.

970

971 Hintze, L. H. and Kowallis, B. J. 2009. The geologic history of Utah Brigham Young University

972 Geology Studies Special Publication 9.

973

974 Huang, Y.Y., Beal, C.M., Cai, W.W., Ruoff, R.S., Terentjev, E.M., 2010. Micro-Raman

975 spectroscopy of algae: Composition analysis and fluorescence background behavior. Biotechnol.

976 Bioeng. 105, 889–898. doi:10.1002/bit.22617

977

978 Izawa, M.R.M., Applin, D.M., Norman, L. and Cloutis, E.A., 2014. Reflectance spectroscopy

979 (350–2500nm) of solid-state polycyclic aromatic hydrocarbons (PAHs). Icarus, 237, pp.159-181.

980

981 Jessberger, E.K. and Castellucci, E.M. and the Gentner team., 2003. GENTNER – a Miniaturised

982 Laser Instrument for Planetary in-situ Analysis. Call for Ideas: Pasteur Instrument Payload for

983 the ExoMars Rover Mission. CI-Pasteur-13.

984

985 Jubb, A.M., Allen, H.C., 2010. Vibrational Spectroscopic Characterization of Hematite,
986 Maghemite, and Magnetite Thin Films Produced by Vapor Deposition. ACS Appl. Mater.
987 Interfaces 2, 2804–2812. doi:10.1021/am1004943
988

989
990 Karwowski, Ł., Helios, K., Kryza, R., Muszyński, A., Drożdżewski, P., 2013. Raman spectra of
991 selected mineral phases of the Morasko iron meteorite. J. Raman Spectrosc. 44, 1181–1186.
992 doi:10.1002/jrs.4340
993

994

995 Košek, F., Culka, A., Drahota, P., & Jehlička, J., 2017. Applying portable Raman spectrometers

996 for field discrimination of sulfates: Training for successful extraterrestrial detection. Journal of

997 Raman Spectroscopy, 48(8), 1085-1093.

998

999 Korablev, O.I., Dobrolensky, Y., Evdokimova, N., Fedorova, A.A., Kuzmin, R.O., Mantsevich,

1000 S.N., Cloutis, E.A., Carter, J., Poulet, F., Flahaut, J. and Griffiths, A., 2017. Infrared

1001 spectrometer for ExoMars: a mast-mounted instrument for the Rover. Astrobiology, 17(6-7),

1002 pp.542-564.

1003

1004 Krause, S., Lewandowski, J., Grimm, N.B., Hannah, D.M., Pinay, G., McDonald, K., Martí, E.,

1005 Argerich, A., Pfister, L., Klaus, J. and Battin, T., 2017. Ecohydrological interfaces as hotspots of

1006 ecosystem processes. Water Resources Research.

1007

1008 Koura, N., Kohara, S., Takeuchi, K., Takahashi, S., Curtiss, L.A., Grimsditch, M., Saboungi, M.-

1009 L., 1996. Alkali carbonates: Raman spectroscopy, ab initio calculations, and structure. J. Mol.

1010 Struct. 382, 163–169. doi:http://dx.doi.org/10.1016/0022-2860(96)09314-3

1011

1012   Laing, J.R., H.C. Robichaud, and E.A. Cloutis, 2016. An assessment of macro-scale in situ

1013   Raman and ultraviolet-induced fluorescence spectroscopy for rapid characterization of frozen

1014   peat and ground ice. International Journal of Astrobiology, 15, 119-126.

1015

1016   Lukačević, I., Gupta, S.K., Jha, P.K., Kirin, D., 2012. Lattice dynamics and Raman spectrum of

1017   rutile TiO2: The role of soft phonon modes in pressure induced phase transition. Mater. Chem.

1018   Phys. 137, 282–289. doi:http://dx.doi.org/10.1016/j.matchemphys.2012.09.022

1019

1020   Mars 2020 SDT, 2013, Committee members: Mustard, J.F. (chair), M. Adler, A. Allwood, D.S.

1021   Bass, D.W. Beaty, J.F. Bell III, W.B. Brinckerhoff, M. Carr, D.J. Des Marais, B. Drake, K.S.

1022   Edgett, J. Eigenbrode, L.T. Elkins-Tanton, J.A. Grant, S. M. Milkovich, D. Ming, C. Moore, S.

1023   Murchie, T.C. Onstott, S.W. Ruff, M.A. Sephton, A. Steele, A. Treiman, 2013, Report of the

1024   Mars 2020 Science Definition Team, 154 pp., posted July, 2013, by the Mars Exploration

1025   Program Analysis Group (MEPAG) at

1026   http://mepag.jpl.nasa.gov/reports/MEP/Mars_2020_SDT_Report_Final.pdf.

1027

1028   Marzo, G.A., oush, T. L., Lanza, N. L., McGuire, P. C., Newso, H. E., Olilla, A. M., and

1029   Wiseman, S. M. 2009. Mineralogy of the inverted channel on the floor of Miyamoto Crater,

1030   Mars. Abstracts 40th Lunar and Planetary Science Conference, abstract 1236.

1031

1032   McClain, M.E., Boyer, E.W., Dent, C.L., Gergel, S.E., Grimm, N.B., Groffman, P.M., Hart,

1033   S.C., Harvey, J.W., Johnston, C.A., Mayorga, E. and McDowell, W.H., 2003. Biogeochemical

1034   hot spots and hot moments at the interface of terrestrial and aquatic

1035   ecosystems. Ecosystems, 6(4), pp.301-312.

1036

1037   McKay, C.P., 2014. Requirements and limits for life in the context of exoplanets. Proceedings of

1038   the National Academy of Sciences, 111(35), pp.12628-12633.

1039

1040   McKeown,N.K.,Bishop,J.L.,NoeDobrea,E.Z.,Ehlmann,B.L.,Parente,M.,Mustard,J.F.,

1041   Murchie,S.L.S.,G.A.,Bibring,J.-P.,Silver,E.A.,2009.Characterizationofphyllosi-

1042   licatesobservedinthecentralMawrthVallisregion,Mars,theirpotentialfor-

1043   mationalprocesses,andimplicationsforpastclimate.J.Geophys.Res.114,1–20.

1044

1045   Mertzman, S.A.,2000. K–Ar results from the southern Oregon-northern California Cascade

1046   Range. Oregon Geology. 62,99–122

1047   Miall, A.D., and C.E. Turner-Peterson, 1989.Variations in fluvial style in the Westwater Canyon

1048   Member, Morrison Formation (Jurassic), San Juan Basin, Colorado Plateau. Sedimentary

1049   Geology, 63, 21-60.

1050

1051   Ming, D.W., Archer, P.D., Glavin, D.P., Eigenbrode, J.L., Franz, H.B., Sutter, B., Brunner, A.E.,

1052   Stern, J.C., Freissinet, C., McAdam, A.C. and Mahaffy, P.R., 2014. Volatile and organic

1053   compositions of sedimentary rocks in Yellowknife Bay, Gale Crater, Mars. Science, 343(6169),

1054   p.1245267.

1055

1056   Mojzsis, S.J. and Arrhenius, G., 1998. Phosphates and carbon on Mars: exobiological

1057   implications and sample return considerations. Journal of Geophysical Research:

1058   Planets, 103(E12), pp.28495-28511.

1059

1060   Nesbitt, H.W. and Young, G.M., 1984. Prediction of some weathering trends of plutonic and

1061   volcanic rocks based on thermodynamic and kinetic considerations. Geochimica et

1062   Cosmochimica Acta, 48(7), pp.1523-1534.

1063

1064   Newsome, N. E., Lanza, N. L., Ollila A. M., Wiseman, S. M., Roush, T. L., Marzo, G. A.,

1065   Tornabene L. L., Okubo, C. H., Osterloo, M. M., Hamilton, V. E., and Crumpler, L. S. 2010.

1066   Inverted channel deposits on the floor of Miyamoto crater, Mars. Icarus 205, pp. 64–72.

1067

1068   Osinski, G.R., Battler, M., Caudill, C.M., Francis, R., Haltigin, T., Hipkin, V.J., Kerrigan, M.,

1069   Pilles, E.A., Pontefract, A., Tornabene, L.L. and Allard, P., 2019. The CanMars Mars Sample

1070   Return analogue mission. *Planetary and Space Science*, *166*, pp.110-130.

1071

1072   Pain, C.F., Clarke, J.D.A., Thomas, M., 2007. Inversion of relief on Mars. Icarus 190, pp. 478–
1073   491.

1074

1075   Pilles, E.A., Cross, M., Caudill, C.M, Francis, R., Osinski, G., Newman, J., Battler, M.,
1076   Bourassa, M., Haltigin, T., Hipkin, V., Kerrigan, M., McLennan, S., Silber, E.A., Williford, K.,
1077   2019. Exploring new models for improving planetary rover operations efficiency through the
1078   2016 CanMars Mars Sample Return (MSR) Analogue Development. Planetary and Space
1079   Science 165, pp.250-259).

1080

1081   Preston, L.J., Izawa, M.R.M. and Banerjee, N.R., 2011. Infrared spectroscopic characterization
1082   of organic matter associated with microbial bioalteration textures in basaltic
1083   glass. Astrobiology, 11(7), pp.585-599.

1084

1085   Preston, L.J., Johnson, D., Cockell, C.S. and Grady, M.M., 2015. Fourier transform infrared
1086   spectral detection of life in polar subsurface environments and its application to Mars
1087   exploration. Applied spectroscopy, 69(9), pp.1059-1065.

1088

1089   Rice, M. S. and Bell, J. F. 2010. Geologic mapping of the proposed Mars Science Laboratory
1090   (MSL) landing ellipse in Eberswalde Crater. Abstracts 41st Lunar and Planetary Science
1091   Conference, Abstract 2524.

1092

1093   Rhind, T., Ronholm, J., Berg, B., Mann, P., Applin, D., Stromberg, J., Sharma, R., Whyte, L.G.
1094   and Cloutis, E.A., 2014. Gypsum-hosted endolithic communities of the Lake St. Martin impact
1095   structure, Manitoba, Canada: spectroscopic detectability and implications for Mars. *International*
1096   *Journal of Astrobiology*, *13*(4), pp.366-377.
1097   Reiche, L.E., Fahey, J., 1962. An improved method for the determination of FeO in rocks and
1098   minerals including garnets. U.S. Geological Survey Bulletin 1144-B, pp. 1-5

1099

1100   Rull, F., Martinez-Frias, J., Rodríguez-Losada, J.A., 2007. Micro-Raman spectroscopic study of
1101   El Gasco pumice, western Spain. J. Raman Spectrosc. 38, 239–244. doi:10.1002/jrs.1628
1102

1103 Rull, F., S. Maurice, I. Hutchison, A. Moral, C. Perez, C. Diaz, M. Colombo, T. Belenguer, G.
1104 Lopez-Reyes, A. Sansano, O. Forni, Y. Parot, N. Sriegib, S. Woodward, C, Howe, N. Tarcea, P.
1105 Rodriguez, L. Seoane, A. Santiago, J.A. Rodriguez-Prieto, J. Medina, P. Gallego, R. Canchal, P.
1106 Santamaria, G. Ramos, J.L. Vago, and the RLS Team,2017.The Raman Laser Spectrometer for
1107 the ExoMars rover mission to Mars. Astrobiology, 17, 627-654.
1108
1109 Schweikert, R.A., Bogen, N.L., Girty, G.H., Hanson, R.E., Merguerian, C., 1984, Timing and
1110 structural expression of the Nevadan orogeny, Sierra Nevada, California. GSA Bulletin ; 95 (8):
1111 967–979. doi: https://doi.org/10.1130/0016-7606(1984)95<967:TASEOT>2.0.CO;2
1112
1113 Sekiya, T., Ohta, S., Kamei, S., Hanakawa, M., Kurita, S., 2001. Raman spectroscopy and phase
1114 transition of anatase TiO2 under high pressure. J. Phys. Chem. Solids 62, 717–721.
1115 doi:http://dx.doi.org/10.1016/S0022-3697(00)00229-8
1116
1117 Skulinova, M., Lefebvre, C., Sobron, P., Eshelman, E., Daly, M., Gravel, J. F., Cormier, J-F.,
1118 Chateaunuef, F., Slater, G., Zheng, W., Koujelev, A.Leveille, R., 2014. Time-resolved stand-off
1119 UV-Raman spectroscopy for planetary exploration. Planetary and Space Science, 92, 88-100.
1120
1121 Sharma, S.K., Angel, S.M., Ghosh, M., Hubble, H.W. and Lucey, P.G., 2002. Remote pulsed
1122 laser Raman spectroscopy system for mineral analysis on planetary surfaces to 66
1123 meters. Applied Spectroscopy, 56(6), pp.699-705.
1124
1125 Sharma, S.K., Misra, A.K., Lucey, P.G., Wiens, R.C. and Clegg, S.M., 2007. Combined remote
1126 LIBS and Raman spectroscopy at 8.6 m of sulfur-containing minerals, and minerals coated with
1127 hematite or covered with basaltic dust. Spectrochimica Acta Part A: Molecular and Biomolecular
1128 Spectroscopy, 68(4), pp.1036-1045.
1129
1130 Stromberg, J.M., Applin, D.M., Cloutis, E.A., Rice, M., Berard, G. and Mann, P., 2014. The
1131 persistence of a chlorophyll spectral biosignature from Martian evaporite and spring analogues
1132 under Mars-like conditions. International Journal of Astrobiology, 13(3), pp.203-223.
1133

1134 Summons, R.E., Amend, J.P., Bish, D., Buick, R., Cody, G.D., Des Marais, D.J., Bromart, G.,

1135 Eigenbrode, J.L., Knoll, A.H. & Sumner, D.Y.,(2011

1136 . Preservation of martian organic and environmental records: final report of the Mars

1137 biosignature working group. Astrobiology 11(2),

1138 157–181

1139

1140 Williams, R.M., Irwin, R.P. and Zimbelman, J.R., 2009. Evaluation of paleohydrologic models

1141 for terrestrial inverted channels: Implications for application to martian sinuous

1142 ridges. Geomorphology, 107(3), pp.300-315.

1143

1144

1145 Williams, R.M.E., Grotzinger, J.P., Dietrich, W.E., Gupta, S., Sumner, D.Y., Wiens, R.C.,

1146 Mangold, N., Malin, M.C., Edgett, K.S., Maurice, S., Forni, O., Gasnault, O., Ollila, A.,

1147 Newsom, H.E., Dromart, G., Palucis, M.C., Yingst, R.A., Anderson, R.B., Herkenhoff, K.E., Le

1148 Mou_elic, S., Goetz, W., Madsen, M.B., Koefoed, A., Jensen, J.K., Bridges, J.C., Schwenzer,

1149 S.P., Lewis, K.W., Stack, K.M., Rubin, D., Kah, L.C., Bell, J.F., Farmer, J.D., Sullivan, R., Van

1150 Beek, T., Blaney, D.L., Pariser, O., Deen, R.G., Team, M.S.L.S., 2013. Martian fluvial

1151 conglomerates at Gale Crater. Science. 340, 1068–1072.

1152
1153 Wray,J.J.,Ehlmann,B.L.,Squyres,S.W.,Mustard,J.F.,Kirk,R.L.,2008.Compositionalstrati-

1154 graphyofclay-bearinglayereddepositsatMawrthVallis,Mars.Geophys.Res.Lett.35.

1155

1156 Vago, Jorge L., Frances Westall, Pasteur Instrument Teams, Landing Site Selection Working

1157 Group, and Other Contributors (2017). Habitability on Early Mars and the Search for

1158 Biosignatures with the ExoMars Rover. Astrobiology, v. 17, p. 471-510. DOI:

1159 10.1089/ast.2016.1533.

1160

1161 Zotov, N., Ebbsjö, I., Timpel, D., Keppler, H., 1999. Calculation of Raman spectra and

1162 vibrational properties of silicate glasses: Comparison between Na2Si4O9 and SiO2 glasses.

1163 Phys. Rev. B. doi:10.1103/PhysRevB.60.6383